UC Santa Cruz
UC Santa Cruz Electronic Theses and Dissertations

Title

Temperature-Dependent Electron Transport in Quantum Dot Photovoltaics

Permalink

https://escholarship.org/uc/item/7rn901nd

Author

Padilla, Derek

Publication Date

2013

Peer reviewed|Thesis/dissertation

UNIVERSITY OF CALIFORNIA

SANTA CRUZ

**TEMPERATURE-DEPENDENT ELECTRON TRANSPORT IN
QUANTUM DOT PHOTOVOLTAICS**

A dissertation submitted in partial satisfaction of the
requirements for the degree of

DOCTOR OF PHILOSOPHY

in

PHYSICS

by

Derek J. Padilla

June 2013

The Dissertation of Derek J. Padilla
is approved:

_____

Professor Sue A. Carter, Chair

_____

Professor Glenn B. Alers

_____

Professor Dave P. Belanger

_____

Tyrus Miller
Vice Provost and Dean of Graduate Studies

Table of Contents

List of Figures

List of Tables

Abstract

Temperature-Dependent Electron Transport in Quantum Dot Photovoltaics

by

Derek J. Padilla

Quantum dot photovoltaics have attracted much interest from researchers in recent years. They have the potential to address both costs and efficiencies of solar cells while simultaneously demonstrating novel physics. Thin-film devices inherently require less material than bulk crystalline silicon, and solution deposition removes the high energy used in fabrication processes. The ease of bandgap tunability in quantum dots through size control allows for simple graded bandgap structures, which is one method of breaking beyond the Shockley-Queisser limit. Power output can also be increased through the process of multiple exciton generation, whereby more than one electron participates in conduction after the absorption of a single photon. In this dissertation work, quantum dot photovoltaics are examined through a range of temperatures. Exploring the current-voltage-temperature parameter space provides insight into the dominant conduction mechanisms within these materials, which is largely not agreed upon. Beginning with PbS quantum dots, changes in device structure are examined by varying the capping ligand and nanoparticle size. This leads similar studies of new, germanium quantum dot devices. Through this understanding, further optimization of device structure can lead to enhanced device performance.

x

Acknowledgments

To the entire Carter Lab, and all family and friends, I thank you for your support: Sue

and Glenn for advising; Yvonne, Chris, and Rebekah for training; Guangmei and Carena

for having great devices essentially on tap; everyone in the UCSC Physics Department

for making this PhD process an enjoyable and rewarding experience; Mom, Dad, and

Lindsay for your unbelievable love and support through it all.

Chapter 1

Introduction

In 1959, Richard Feynman gave a talk to the American Physical Society at Caltech entitled *There's Plenty of Room at the Bottom.* In it he foretold of future engineering efforts taking advantage of the quantum properties of the small scale: "[A]s we go down and fiddle around with the atoms down there, we are working with different laws, and we can expect to do different things. We can use, not just circuits, but some system involving the quantized energy levels" [1]. In the 50 years since his talk laid the conceptual foundation for nanotechnology, we have seen many of his ideas realized: layered semiconductor devices are manufactured with atomic-layer precision [2]; structures on the nanometer scale within layers are manufactured using electron beam lithography with much higher resolution than photolithography due to the shorter electron wavelength [3]; microscopy has advanced to seeing individual atoms through the use of scanning tunneling microscopes [4], with those same STMs being able to manipulate individual atom placement as seen in Figure 1.1 where xenon atoms are arranged

on a nickel surface spelling out the name of the employer of the STM inventors [5].

The fundamental qualifier of nanotechnology is not so much the physical dimensions of the system being on the order of nanometers, but that physical properties of these structures become sensitive to changes of scale, largely due to quantum mechanical effects taking over from the classical, macroscopic properties. This occurs around the nanometer scale in solids, which is on the order of the Bohr exciton radius. Beginning with a bulk, three-dimensional solid, decreasing one dimension until there is a very thin sheet yields a nanolayer, where the quantum confinement affects only one dimension. Quantum confinement in two dimensions leaves a one-dimensional nanowire. And a nanoparticle (NP) is the zero-dimensional result of quantum confinement in all three directions.

This dissertation focuses on the application of semiconducting nanoparticles, or quantum dots (QDs), to photovoltaic devices. By requiring less material than bulk semiconducting crystals used in conventional solar cells, these devices have the ability to reach a lower dollar-per-Watt figure once optimized. A fundamental understanding of the basic electron transport mechanism is required to find potential pathways to improved efficiencies in the devices. To this end, exploring the current-voltage-temperature parameter space elucidates dominant conduction models and possible power losses in the QD solar cells.

Much of the understanding of QD devices builds upon that of bulk semiconductors and their devices. The presented content begins with a discussion of bulk properties, which leads to modifications required for a more complete understanding of
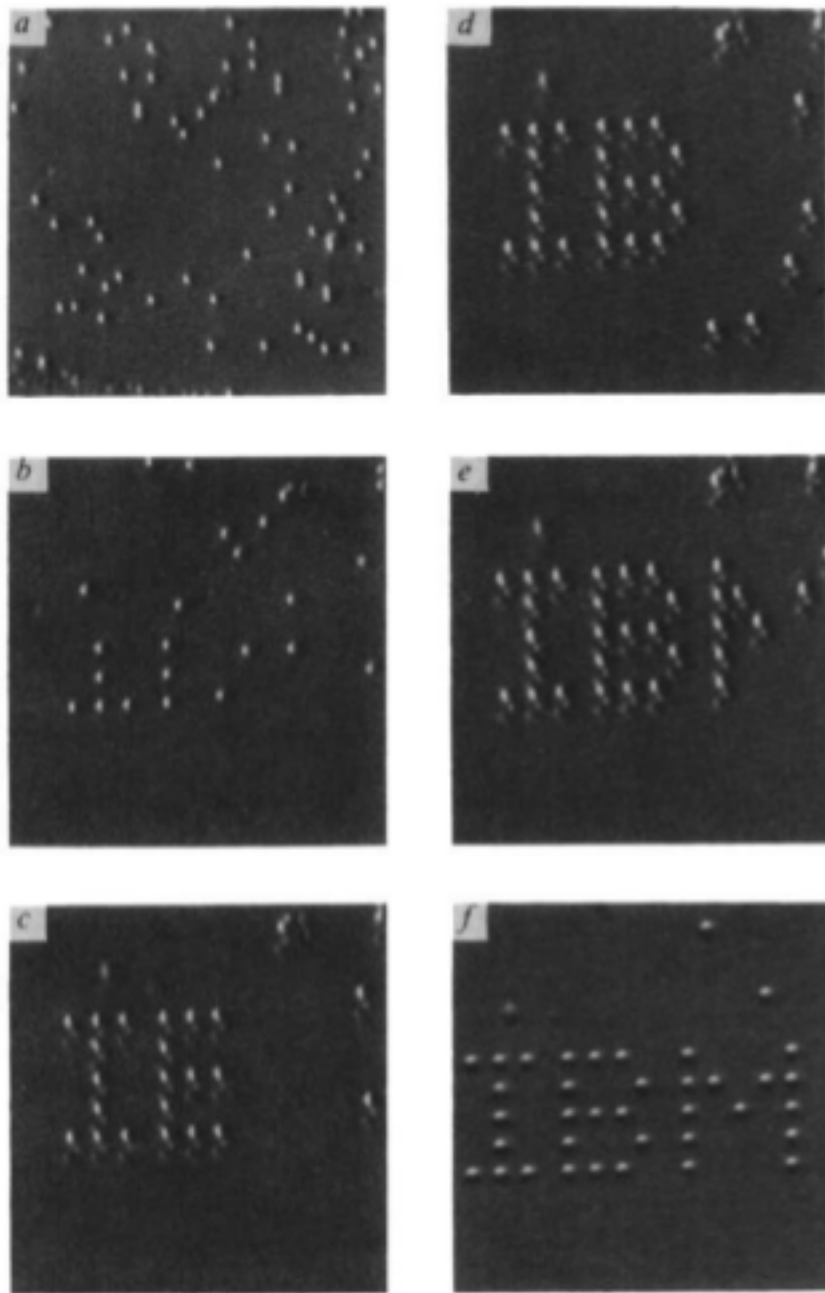
Figure 1.1: Scanning tunneling microscope positions individual atoms to spell the name of the inventors' employer.

3

QDs. Chapter 3 explores what happens when two different types of semiconductor are put in contact, which leads to the semiconductor diode. The following chapter presents the interaction of semiconductor devices with incident sunlight. The relevant properties of sunlight to solar cells and a brief exploration of current solar cell technologies is followed by their relation to QD photovoltaics (PV). Experimental methods used in the current study is given in chapter 5, with the results of these studies presented in chapters 6 and 7.

Chapter 2

Semiconductor Properties

Before examining quantum confinement effects in quantum dots, a discussion of bulk properties of materials is necessary to understand semiconductors and basic device physics. For photovoltaic (PV) devices, there are two classes of physical properties that are of interest to researchers—electronic, and optical—both of which are largely understood through the band structure of the materials.

2.1 Electronic Bands in Bulk Materials

A conceptual picture of band formation begins with two electrons in spatially-separated quantum states of equal energy. As the electrons are brought closer together, the states hybridize and split into two different energy levels due to their interaction. When N such electrons are brought close to each other, the states split into N distinct energy levels. When N is on the order of Avogadro's number, these differences in energy are so small that the states are considered to make up a continuous band of allowed

5
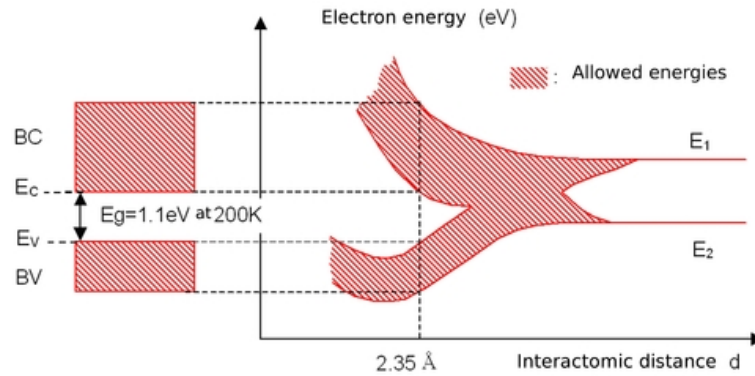
Figure 2.1: As the lattice constant for silicon decreases, bands of allowed energies are created. Higher energy states split, potentially leaving a gap of forbidden energy values.

energies.

This band formation can be interpreted as a demonstration of the Pauli exclusion principle in that forcing electrons into spatially overlapping states requires a splitting of the energy levels since no two electrons can occupy the same quantum state. In a solid, as the inter-atomic spacing, or lattice constant, decreases, the outer electron states split into bands due to their significant spatial overlap. Lower-energy electron states likely do not split since their interaction and spatial overlap is much smaller. Two bands may broaden to the point of overlapping in energy, or remain energetically separated leaving a gap of forbidden values for electron energy. Figure 2.1 demonstrates this property for silicon. It is the formation of this energy gap that gives rise to the incredibly large range of electrical conduction abilities across materials.

Even without a quantitative analysis, we can see how this simple band picture affects conduction by considering the number of available electrons in a solid compared to the number of available energy states. At low temperatures, electrons occupy the
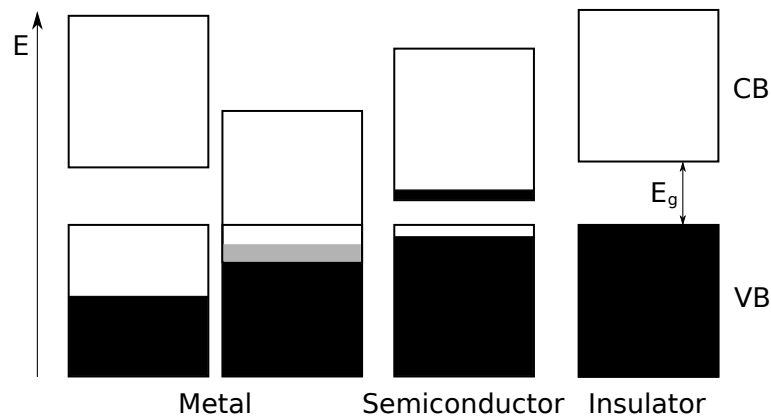
Figure 2.2: The filling of electron energy bands for different classifications of materials.

lowest energy state available to them and fill increasing energy states from there. In a metal, the number of electrons is less than the number of states in the highest occupied band allowing for easy conduction through the solid since there will always be a state to move into with an applied electric field, as seen in Figure 2.2. The energy of the highest occupied state is called the Fermi energy. An insulator has just enough states in a band to be occupied completely by all valence electrons of the constituent atoms. This band is therefore called the valence band. The next highest state exists across the band gap and requires a significant excitation energy to reach the band to participate in conduction. These higher energy states exist in the conduction band. The required excitation can come from a very high applied field, the absorption of light, or thermal interactions with crystal vibrations (phonons), however these require such high temperatures that it is unlikely that any electrons will flow before significant electric field is present.

If the energy gap is small enough such that thermal vibrations allow for some of the lower conduction band states to be occupied at moderate temperatures, the material

is called a semiconductor. The band gap is still present but typically is no higher than several electron volts. Silicon, for example, has a band gap of 1.1 eV. These materials exhibit conduction at moderately applied fields while at room temperature. The Fermi energy for a pure insulator or semiconductor is one half of the band-gap energy.

The above description qualitatively explains the presence of energy bands in a solid, however a more complete picture is obtained when considering the quantum mechanical wavefunctions of electrons with the crystal's atomic potential in addition to including the spatially finite dimensions of a material sample. Several good introductory sources exist that derive electronic bands from periodic finite square wells (the Kronig-Penny model) [6] and repeating delta functions [7]. A qualitative result of these calculations is that energy gap sizes increase with increasing potential well strength, which is realized in semiconductors made of smaller atoms, and compound semiconductors [8]. These one-dimensional models provide simple dispersion relations between electron energy and momentum p or wavenumber k, an example of which is shown in Figure 2.3. The flat bands of Figure 2.2 are now given structure in momentum-space, the differences of which lead to material classifications based on positions of the valence and conduction bands.

If the top of the valence band corresponds to the same k-value of the bottom of the conduction band, the material is said to have a direct gap (cf. Figure 2.4). If the k values are different, it is an indirect gap. This distinction has implications for light absorption and emission. For an incident photon of energy equal to the energy gap to be absorbed, the total energy *and momentum* must be conserved. The electron absorbs

8
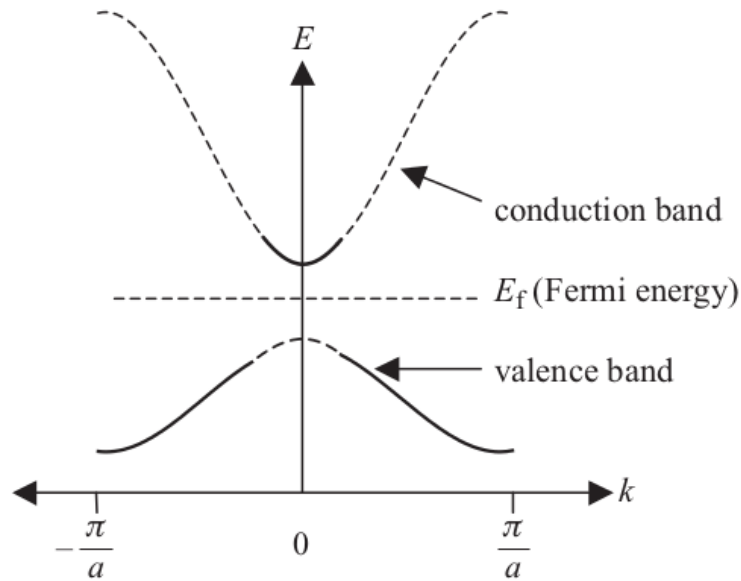
Figure 2.3: The *E-k* dispersion relationship shown for the solutions to a simple 1D periodic potential presented in the reduced zone scheme.

the energy, transferring from the top of the valence to the bottom of the conduction band. But for visible light, the photon doesn't carry enough momentum to have it be conserved ($p=h/\lambda$). The transition requires the excited electron to simultaneously interact with a phonon to completed the absorption process, drastically decreasing the probability of this occurring. Because of this, the absorption coefficient for indirect gap semiconductors is much lower than direct gap materials.

Silicon is an example of an indirect gap semiconductor, and therefore single crystalline Si solar cells require a much thicker absorbing layer than direct gap counterparts (e.g. GaAs or CdTe) to ensure all incident light is absorbed. Figure 2.5 shows the band structure of silicon. The top of the valence band is at the origin with the energy gap E_g being offset along the <100> crystal momentum direction. There clearly
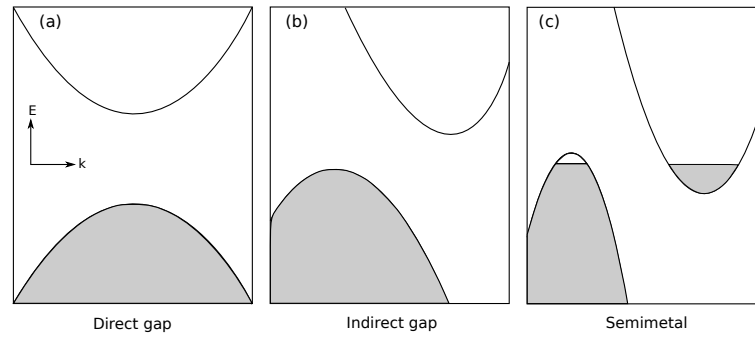
Figure 2.4: The filling of bands including the k-space dependence.

exist several other bands deriving from the interplay between the electronic structure of atomic silicon and the bulk crystal structure of the atoms existing as a diamond lattice. In contrast to the indirect gap of silicon, the electronic band structure of CdTe is shown in Figure 2.6. This direct band gap material has a gap size of 1.58 eV as is used in many thin film photovoltaic applications.

2.2   Charge Carriers in Solids

As stated earlier, for the case of semiconductors, the highest occupied band (at 0 K) is filled completely by electrons. As the temperature increases, electrons have a non-zero probability of being thermally excited across the band gap into the conduction band, where they freely move throughout the crystal. The empty state they leave behind can itself transit through the crystal lattice acting as an effective positive charge carrier called a hole. The two particles (electron and hole) are bound to one another through the Coulomb interaction. The effective size of their bound state is called the Bohr exciton radius. A significant challenge to developing effective photovoltaic devices is

Energy   300 K $E_g = 1.1$ eV
                                    $E_L = 2.0$ eV
                                    $E_X = 1.2$ eV
                                    $E_{so} = 0.044$ eV
                                    $E_{\Gamma 1} = 3.4$ eV
                                    $E_{\Gamma 2} = 4.2$ eV
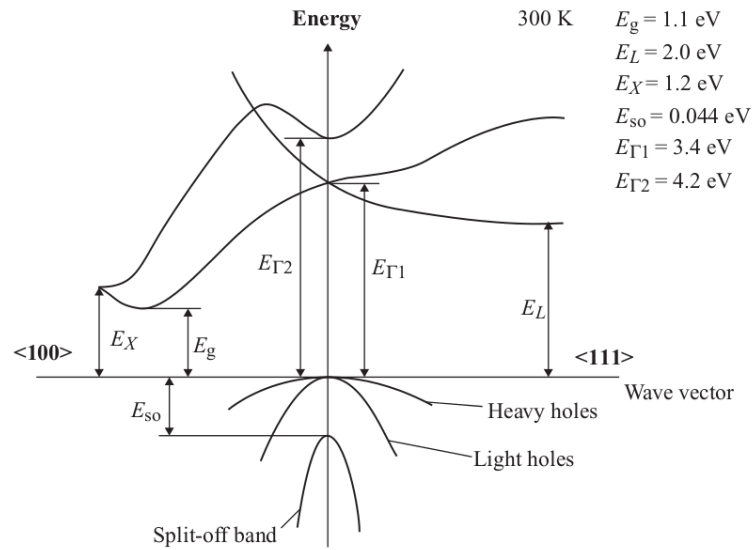
Figure 2.5: Electronic band structure of silicon demonstrating the indirect band gap energy of 1.1 eV.

separating these two charge carriers and extracting them out of the device at opposite electrodes.

In a pure semiconducting material, each electron in the conduction band is matched by a hole in the valence band. This is called an intrinsic semiconductor, with Fermi energy at half the band gap. Electronic properties of materials depend strongly on the concentration of electrons n and holes p within a sample. (For intrinsic materials, $n_i = p_i$.) Therefore, being able to tune these parameters is of great value to device engineering. This is done through the process of doping. Taking, for example, a Group IV element like silicon with four valence electrons, and embed into the crystal a Group V element like phosphorous with five valence electrons, and the extra valence electrons are loosely bound to the bulk crystal's atoms as seen in Figure 2.7. This allows them to easily participate in conduction by introducing an available state near

11
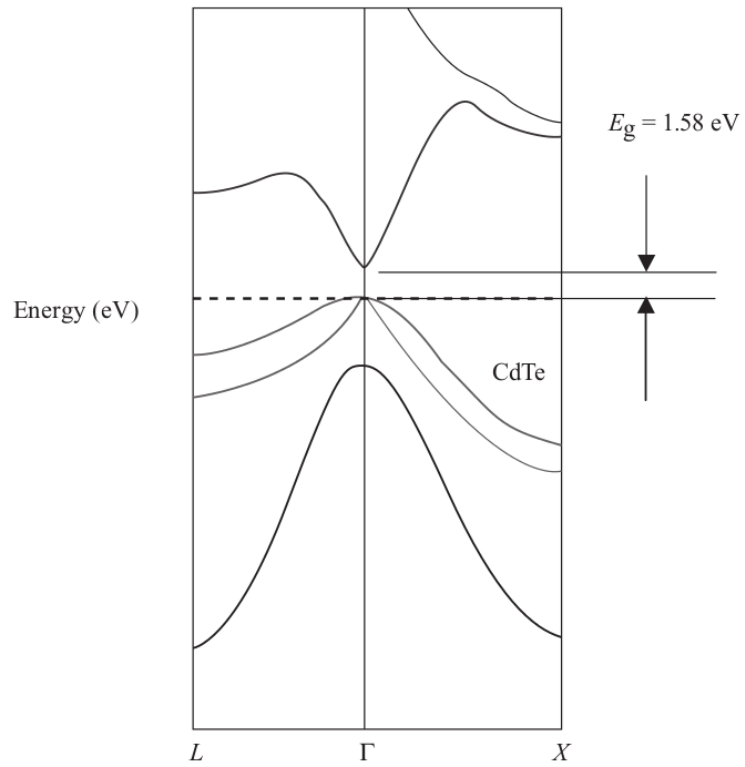
Figure 2.6: Electronic band structure of CdTe demonstrating the direct band gap energy of 1.58 eV.
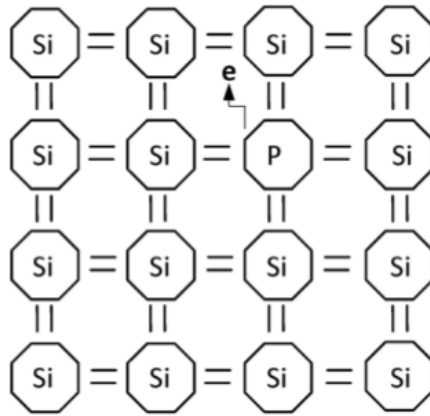
Figure 2.7: The doping of a silicon crystal by introducing phosphorus provides extra electrons to participate in charge conduction.

the bottom of the conduction band called a donor state. The Group V atoms are donors. This requires little excitation energy to be promoted and participate in conduction.

If instead of an element with one extra valence electron, we embed atoms of a Group III element such as aluminum, which has one fewer valence electron. This effectively introduces an empty electron state within the band gap near the top of the valence band allowing electrons to easily be excited into this acceptor state due to the doping from the acceptor atoms. This excitation leaves behind a hole that is able to participate in conduction through the valence band.

2.3 Density of States

The doping of semiconductors changes the probabilities for charge carriers to participate in conduction, and in order to quantify this probability we need the density of states within the semiconductor as a function of electron energy. This density of

states combined with the probability distribution of a state at a particular energy being occupied will provide the overall density of charge carriers as a function of energy.

The possible energy states available in a quantum mechanical system derives from the solutions to Shrödinger's equation. The semiconducting crystal can be modeled as a three-dimensional infinite square well of dimensions a, b, c, with $V=0$ inside and $V=\infty$ outside the boundaries. Modifications to take into account the periodic nature of the crystal potential will be addressed at the end. With this simple crystal, the electrons are essentially free particles whose wavefunction solves

$$-\frac{\hbar^2}{2m}\nabla^2\Psi(x,y,z) = E\Psi(x,y,z),\qquad(2.1)$$

with $\Psi=0$ at the boundaries. The solution is a normalized product of sine functions of quantized wavelengths given by

$$\lambda_x = \frac{2a}{n_x},\qquad(2.2)$$

with n_x being a positive integer, and similar solutions for the y and z directions. The energy eigenvalue solutions are given by

$$E = \frac{\hbar^2\pi^2}{2m}\left[\left(\frac{n_x}{a}\right)^2 + \left(\frac{n_y}{b}\right)^2 + \left(\frac{n_z}{c}\right)^2\right].\qquad(2.3)$$

If electrons are put into the crystal at absolute zero temperature, they begin to fill states from the lowest energy upward. Each unique combination of (n_x, n_y, n_z) is

a quantum state to be occupied by two electrons.[1] At typical energies E, the volume in reciprocal lattice space that contains all accessible states is considered much larger than the unit cell volume of $1/abc$. This volume is an ellipsoid with semi-major axes equal to

$$\frac{n_x}{a} = \frac{n_y}{b} = \frac{n_z}{c} = \sqrt{\frac{2mE}{\hbar^2 \pi^2}}. \tag{2.4}$$

Filling this volume with electrons whose energy is less than E, we find that the number of states available is two times (counting spin) one eighth (positive octant only — $n{>}0$) the volume of the ellipsoid divided by the volume of one state (the unit cell):

$$\# \text{ of states} = \frac{2 \left(\frac{1}{8}\right) \left[\frac{4}{3}\pi \left(\frac{2mE}{\hbar^2 \pi^2}\right)^{3/2}\right]}{1/abc}. \tag{2.5}$$

If we divide this number of states that are occupied by electrons of energy less than E by the volume of the box abc, we arrive at the number of electrons per unit volume within the semiconductor:

$$n(E) = 2 \left(\frac{1}{8}\right) \left[\frac{4}{3}\pi \left(\frac{2mE}{\hbar^2 \pi^2}\right)^{3/2}\right]. \tag{2.6}$$

Finally, the density of states for a given energy E is given by

$$N(E) = \frac{dn}{dE} = \frac{\pi}{2} \left(\frac{2m}{\hbar^2 \pi^2}\right)^{3/2} E^{1/2}. \tag{2.7}$$

---

[1] Each point can hold two electrons since they each can have spin equal to +1/2 or -1/2, which is another valid quantum number to still satisfy the Pauli exclusion principle.

This derivation began by assuming the semiconducting crystal is a potential well with $V=0$ throughout, which yields a parabolic dispersion relationship. This was implied in Equation 2.3 using $k=2\pi/\lambda$ and the quantized wavelengths of the wavefunctions. A more accurate picture includes the periodic potential of the crystal's constituent atoms. From this periodic potential, the E-k dispersion relationships for states near the bottom of the conduction and top of the valence bands can be approximated by parabolas yielding the same $E \propto k^2$ relationship. A modification is required, however, taking into account the curvature of this parabola being different than that of a free charge carrier. This is done by replacing the mass with the effective mass of the charge carrier given by

$$m^* = \frac{\hbar^2}{\frac{d^2E}{dk^2}}.$$ (2.8)

This change conceptually reflects the electron's ability to respond to an electric field through Newton's second law. The mass m in the density of states equation also needs to be replaced by the effective mass m^*:

$$N(E) = \frac{dn}{dE} = \frac{\pi}{2}\left(\frac{2m^*}{\hbar^2\pi^2}\right)^{3/2} E^{1/2}.$$ (2.9)

With this density of states, we need to determine which of these states is being occupied by electrons. This requires the use of Boltzmann statistics while considering the interaction of a phonon promoting an electron to an empty state of higher energy. This empty-state requirement is a result of the Pauli exclusion principle.
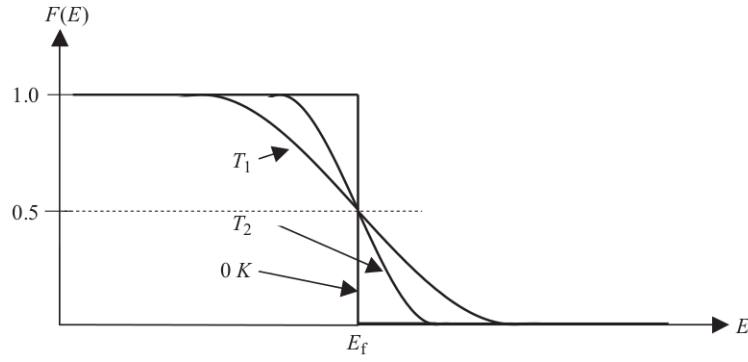
Figure 2.8: The Fermi-Dirac distribution for three temperatures. At 0 K, the distribution is a step function. As temperature increases, the step changes into a gradual slope with high energy tail of non-zero probability. The Fermi energy is defined as that which has a 50% chance of being occupied.

The end result is called the Fermi-Dirac distribution given by

$$f(E) = \frac{1}{1 + \exp\left(\frac{E - E_f}{kT}\right)}. \tag{2.10}$$

The Fermi energy E_f appears, being defined as the energy at which there is a 50% chance of the state being occupied. Figure 2.8 shows the Fermi distribution for several temperatures $T_1 > T_2 > 0$ K. As temperatures increase, there is a higher probability of states with high energy of being populated by electrons, as seen by the tail of the distribution at larger E.

Using Equations 2.9 and 2.10, the density of electrons within the conduction band can be determined:

$$n = \int_{E_g}^{\infty} N(E - E_g)f(E)dE, \tag{2.11}$$

17

where the top of the valence band is chosen to be $E=0$ and the bottom of the conduction band is E_g above that. The upper limit is technically the highest energy level of the conduction band, but in most cases, this is significantly higher than energies obtainable by electrons and is therefore taken to be at infinity, which allows for analytical solutions to the integral:

$$n_0 = 2 \left(\frac{2\pi m_e^* kT}{h^2} \right)^{3/2} \exp\left(\frac{-(E_c - E_f)}{kT} \right) = N_c \exp\left(\frac{-(E_c - E_f)}{kT} \right). \qquad (2.12)$$

This solution assumes that the Fermi level is much farther from the conduction band edge than thermal energy kT. The prefactor N_c is the effective density of states near the conduction band edge. A similar result is obtained for the concentration of holes in the valence band:

$$p_0 = 2 \left(\frac{2\pi m_h^* kT}{h^2} \right)^{3/2} \exp\left(\frac{-(E_f - E_v)}{kT} \right) = N_v \exp\left(\frac{-(E_f - E_v)}{kT} \right). \qquad (2.13)$$

The charge density convolving the density of states and the Fermi-Dirac distribution is shown in Figure 2.9.

These charge densities are valid for equilibrium conditions as denoted by the subscript zero. That is, the device is at constant temperature, in the dark, with no applied field. The equilibrium condition is compared to the steady state condition, where a sample with constant current or constant generation of electron-hole pairs (EHPs) being exactly balanced by recombination.

18
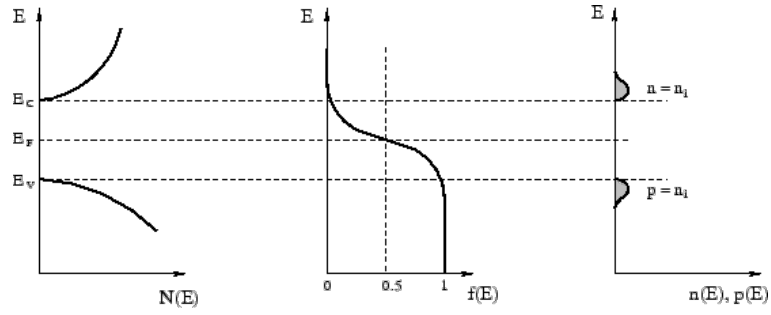
Figure 2.9: The density of states as a function of energy combined with the Fermi-Dirac distribution provides the density of electrons in the conduction band and holes in the valence band.

For an intrinsic semiconductor $n_i = p_i$ and setting Equation 2.12 equal to 2.13, with $E_v = 0$ as our reference energy, we can find the Fermi level:

$$E_f = \frac{E_g}{2} + \frac{kT}{2} \ln \frac{N_v}{N_c}. \tag{2.14}$$

Typically, the second term is much smaller than $E_g/2$ and the Fermi energy lies in the middle of the band gap.

The product of electron and hole concentration is given by

$$n_0 p_0 = N_c N_v \exp\left(\frac{-E_g}{kT}\right), \tag{2.15}$$

and using the fact that $n_i = p_i$ gives the intrinsic carrier concentration for a semiconductor:

$$n_i = p_i = \sqrt{N_c N_v} \exp\left(\frac{-E_g}{2kT}\right). \tag{2.16}$$

19

2.4 Extrinsic Materials

Using the discussion of semiconductor doping from Section 2.2, a quantitative value for the difference in energy between conduction and valence band edges and the Fermi energy can be determined from the above charge density equations. Typical this is done assuming that the cell is warm enough that all donors or acceptors are ionized, but not so warm that the intrinsic carriers are contributing significantly to the total carrier concentration. At room temperature in most materials, these are indeed valid assumptions leading to an approximately constant concentration of carriers. Upon cooling, the concentration drops from this constant value but remains above the intrinsic value since not all donors or acceptors may be ionized. These results are summarized below.

- For n-type semiconductors:

$$n_0 = N_d \qquad p_0 = \frac{n_i^2}{N_d} \qquad E_c - E_f = kT \ln \frac{N_c}{n_0} \tag{2.17}$$

- For p-type semiconductors:

$$p_0 = N_a \qquad n_0 = \frac{n_i^2}{N_a} \qquad E_f - E_v = kT \ln \frac{N_v}{p_0} \tag{2.18}$$

2.5 Non-Equilibrium Conditions

The above description is valid for semiconductors (intrinsic or extrinsic) under equilibrium conditions. If the semiconductor is illuminated or an electric field is applied, this condition no longer holds and the charge carrier concentrations much therefore be

modified.

2.5.1 Quasi-Fermi Energy Levels

Equations 2.12 and 2.13 can be rewritten with the material's Fermi energy being replaced by the quasi-Fermi energies F_n and F_p, which are different than each other and differ from the original Fermi energy E_f. These result from excess electron-hole pairs being generated under illumination or band tilting due to the applied field affecting which states are likely to be occupied by a charge carrier. The quasi-Fermi energy differences can be found from

$$n = N_c \exp\left[\frac{-(E_c - F_n)}{kT}\right] \qquad p = N_v \exp\left[\frac{-(F_p - E_v)}{kT}\right]. \qquad (2.19)$$

The charge densities n and p are adjusted from their equilibrium values through adding a Δn or Δp from e.g. EHP generation rates and charge carrier lifetimes. Generally, for n-type materials, $F_n \sim E_f$ while F_p decreases significantly towards the valence band. Similarly for p-type materials, $F_p \sim E_f$, with F_n increasing towards the conduction band. This can be seen by considering the originally low concentration of minority carriers in the equilibrium condition being increased by several orders of magnitude by the EHP production.

The product of carrier concentrations is given by

$$np = N_c N_v \exp\left(\frac{F_n - F_p - E_g}{kT}\right) = n_0 p_0 \exp\left(\frac{F_n - F_p}{kT}\right), \qquad (2.20)$$

21

which leads to the difference in quasi-Fermi energies being

$$F_n - F_p = kT \ln \left(\frac{np}{n_0 p_0} \right).$$
(2.21)

2.5.2 Applied Electric Fields: Carrier Drift

By connecting two electrodes across a semiconductor with a potential difference V between them, an electric field is present causing charges to flow. Using Ohm's law,

$$J = \sigma \mathcal{E},$$
(2.22)

and the definition of the current density,

$$J = \frac{1}{A} I = \frac{1}{A} \frac{dQ}{dt} = \frac{1}{A} \frac{nqA dx}{dt} = nqv,$$
(2.23)

the relationship between drift velocity v and the applied electric field $\mathcal{E}$ is given by

$$\mathcal{E} = \frac{nqv}{\sigma}.$$
(2.24)

The drift velocity is limited by scattering of charge carriers off of phonons or lattice impurities with a characteristic scattering time given by

$$\tau = \frac{vm^*}{q\mathcal{E}} = \frac{\mu m^*}{q},$$
(2.25)

introducing the charge carrier mobility μ, which may differ between holes and electrons requiring their respective effective mass to be used in Equation 2.25. This allows us to rewrite the total drift current density as a combination of that due to electrons and holes

$$J_{drift} = J_n + J_p = qn\mu_n\mathcal{E} + qp\mu_p\mathcal{E}. \tag{2.26}$$

In addition to examining the charge carriers' motion arising from their responses to an applied field through the mobility and conductivity relations above, the flat bands of the semiconductor in Figure 2.2 are tilted in the applied field providing another visualization of charge transport. From the elementary relation between field and potential given by,

$$\mathcal{E} = -\nabla V, \tag{2.27}$$

the presence of a constant applied field $\mathcal{E}$ leads to the tilting of the energy bands as shown in Figure 2.10. The electrons and holes seek lower energy states moving towards the electrodes creating the charge current. Note that the Fermi energy level does not tilt since the material is still in thermodynamic equilibrium.

2.5.3 Optical Generation

In thermal equilibrium with carrier densities n_0 and p_0, each EHP created is matched by a recombination. This is quantified by the thermal generation rate G_{th} and recombination rate R being equal.

This equilibrium can be disturbed by illuminating the semiconductor with

23
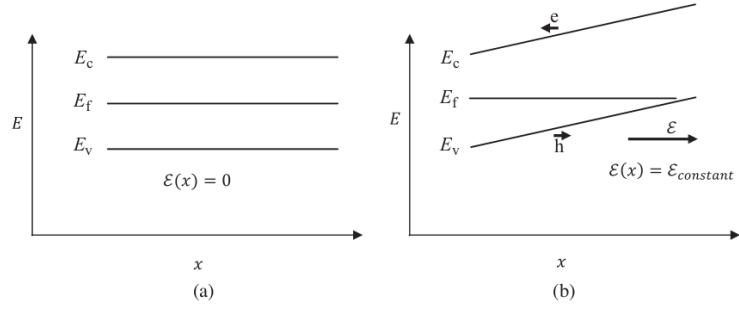
Figure 2.10: (a) Flat band diagram of intrinsic semiconductor with no applied field. (b) After the application of electric field $\mathcal{E}$, the bands tilt with slope equal to the field. Electrons seek lower energy states and move in the opposite direction of the hole flow creating current through the material.

photons of higher energy than the bandgap creating extra *optically* generated EHPs. For incident photon flux $f(\lambda)$ upon a surface with reflectance $r(\lambda)$ and absorption coefficient $\alpha(\lambda)$, the generation rate at a given depth below the surface x is

$$G_{op}(x) = \int (1 - r(\lambda)) \, f(\lambda)\alpha(\lambda)e^{-\alpha x} d\lambda. \tag{2.28}$$

This indicates that most EHP generation occurs at the surface of the material and exponentially decays as the depth increases. The band-gap dependence appears in the $\alpha(\lambda)$ term where an abrupt increase in absorption at $\lambda = hc/E_g$ occurs. For quantum dot films, this is typically seen as an exciton peak in the absorption spectrum, which is the manifestation of the high probability of an electron being excited from the highest hole state 1S(h) within the quantum well to the lowest electron state 1S(e). This generation rate G_{op} leads to a time-dependent excess carrier density $\delta n(t)$ for electrons and $\delta p(t)$ for holes. Illuminating for much longer than a characteristic recombination

24

time τ_n, the excess carrier density reaches a steady-state value Δn. Similar terms exist for hole density.

The recombination time is minority-carrier-limited since both an electron and hole are required for recombination to occur. Minority carrier lifetime τ is a combination of three recombination mechanism lifetimes: radiative, Auger, and Shockley-Read-Hall (SRH) recombination. The total lifetime is the harmonic sum of each individual lifetime:

$$\frac{1}{\tau} = \frac{1}{\tau_{rad}} + \frac{1}{\tau_{Aug}} + \frac{1}{\tau_{SRH}}. \tag{2.29}$$

Radiative recombination occurs when a conduction-band electron recombines with a valence-band hole emitting a photon in the process—essentially the reverse of optical absorption. Similarly, this is more likely to occur in direct band gap materials. Since the photon's energy will be close to the band gap energy it is weakly absorbed. Auger recombination involves three particles: the band-to-band recombination of an EHP, but instead of emitting a photon, the energy is transferred to another charge carrier which thermally relaxes back to the band edge. SRH recombination occurs when an electron, for example, becomes trapped in a mid-gap state and recombines with a hole while trapped. This is more likely to occur in deep states rather than shallow since the electron could easily be re-excited out of the trap if near the conduction band. These traps occur in crystalline solids due to defects or surface states. All three processes are schematically shown in Figure 2.11. The steady-state conditions are summarized as
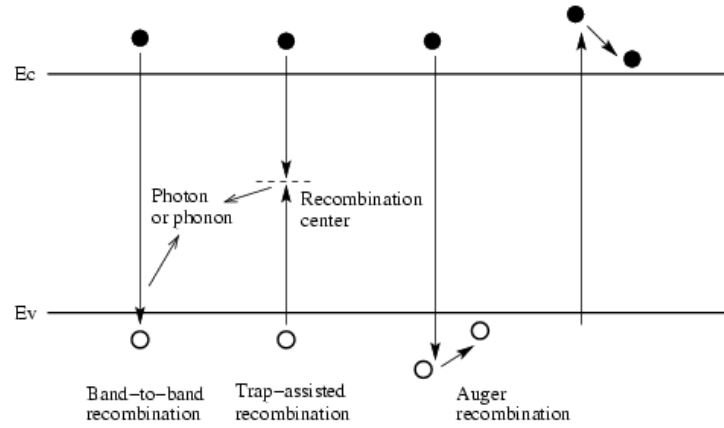
Figure 2.11: Three recombination mechanisms. The band-to-band or radiative, and trap-assisted or SRH, processes involve two charge carriers, while Auger recombination involves a third.

follows:

$$n = n_0 + \Delta n = n_0 + G_{op}\tau_n \qquad p = p_0 + \Delta p = p_0 + G_{op}\tau_p. \qquad (2.30)$$

2.5.4 Diffusion Current

With no applied electric field, the total drift current density is zero. However, charge still flows through semiconductors due to diffusion processes. When a gradient in charge density exists, charge carriers follow Fick's first law of diffusion, which states that particles diffuse from areas of high concentration to lower concentration. This flow of charge carriers leads to a diffusion current density given by

$$J_{diff} = qD_n\nabla n - qD_p\nabla p. \qquad (2.31)$$

D_n and D_p are the diffusion coefficients for electrons and holes, respectively. This diffusion will occur until a uniform charge density profile exists.

2.5.5 The Einstein Relation and Continuity Equations

If the semiconductor has a doping profile of, say, increasing acceptor states such that the conduction and valence bands vary linearly across the sample in the x direction, a diffusion current is present trying to equalize the charge density. This unequal doping also establishes an internal electric field, which creates a drift current from Equation 2.26. In equilibrium, these two currents will be equal and opposite to each other, and, looking at holes only,

$$J_{diff,p} = -J_{drift,p} \tag{2.32}$$

$$-qD_p\frac{dp(x)}{dx} = -qp(x)\mu_p\mathcal{E}(x). \tag{2.33}$$

Since p now depends on position x, and the only term in Equation 2.13 that changes with position is E_v since, in equilibrium, the Fermi energy is constant,

$$-qD_p\frac{N_v}{kT}\exp\left(\frac{-(E_f - E_v(x))}{kT}\right)\frac{dE_v}{dx} = -q\mu_pN_v\exp\left(\frac{-(E_f - E_v(x))}{kT}\right)\frac{1}{q}\frac{dE_v}{dx}$$

$$\frac{D_p}{\mu_p} = \frac{kT}{q}, \tag{2.34}$$

which is the well-known Einstein relation between the diffusion coefficient and carrier mobility. For electrons, a similar derivation yields

$$\frac{D_n}{\mu_n} = \frac{kT}{q}. \tag{2.35}$$

When not in equilibrium the total current density through the material is a combination of electron and hole drift and diffusion current densities:

$$
\begin{aligned}
J &= J_n + J_p & (2.36) \\
&= J_{diff,n} + J_{drift,n} + J_{diff,p} + J_{drift,p} & (2.37) \\
&= qD_n\nabla n + qn\mu_n\mathcal{E} - qD_p\nabla p + qp\mu_p\mathcal{E}. & (2.38)
\end{aligned}
$$

Any divergence of the current density from a point within the material is the result of a difference in particle generation and recombination and a change in carrier density at that point. This is shown in the continuity equation

$$\nabla \cdot J = -q(G - R_n - \frac{\partial n}{\partial t}) + q(G - R_p - \frac{\partial p}{\partial t}), \tag{2.39}$$

where G is the generation rate of EHPs and

$$
\begin{aligned}
R_n &= \frac{p_n - p_{n0}}{\tau_p} = \frac{\Delta p_n}{\tau_p} & (2.40) \\
R_p &= \frac{n_p - n_{p0}}{\tau_n} = \frac{\Delta n_p}{\tau_n} & (2.41)
\end{aligned}
$$

28

are the recombination rates in n- and p-type materials that depend on the minority carrier lifetimes and concentrations respectively.

Considering the diffusion of charge carriers through a semiconductor in one dimension under steady-state conditions ($G=\partial n/\partial t=0$) and combining Equations 2.39 and 2.41, the carrier steady-state diffusion equation for excess holes is given by

$$\frac{d^2\delta p}{dx^2} = \frac{\delta p}{D_p \tau_p}, \tag{2.42}$$

and similarly for electrons,

$$\frac{d^2\delta n}{dx^2} = \frac{\delta n}{D_n \tau_n}. \tag{2.43}$$

If excess carriers of time-independent concentration Δp and Δn exist at $x=0$, the above differential equations each have exponential solutions of the form

$$\delta p = \Delta p \exp\left(\frac{-x}{\sqrt{D_p \tau_p}}\right) = \Delta p \exp\left(\frac{-x}{L_p}\right) \tag{2.44}$$

$$\delta n = \Delta n \exp\left(\frac{-x}{\sqrt{D_n \tau_n}}\right) = \Delta n \exp\left(\frac{-x}{L_n}\right) \tag{2.45}$$

which introduces the diffusion lengths for both holes and electrons:

$$L_p^2 = D_p \tau_p \qquad L_n^2 = D_n \tau_n. \tag{2.46}$$

2.6   Quantum Dots

The above discussion began with the density of states of bulk semiconductors. When a semiconducting crystal is reduced in size to several nanometers in all dimensions through a decrease in the number of atoms, this density of states loses its continuous nature and begins to take on properties of the constituent atoms. Being quantum in nature, the smaller crystals have discretized energy states rather than the continuous bands of the bulk. The fundamental quantum property of these crystals arise from treating the surface as a boundary to a quantum well. Solving the Shrödinger equation for the well follows very similarly to Section 2.3 above for the bulk crystal, however, a fundamental difference is the lack of nearby atoms to form the continuous bands of the bulk.

2.6.1   Quantum Confinement

In bulk semiconductors, the EHPs generated thermally or optically are bound states, which can travel through the crystal as a pseudo-atom called an exciton. This is compared to the bound states of an electron and proton in a hydrogen atom, but since the effective mass of the hole is dramatically less than that of a proton, the Bohr radius is significantly affected. The exciton Bohr radius is given by

$$r_B = \frac{\hbar^2 \epsilon}{q^2} \left(\frac{1}{m_e^*} + \frac{1}{m_h^*} \right). \tag{2.47}$$

As dimensions of semiconductor crystals approach this length scale, quantum effects begin to take hold and the energy required to create an EHP increases, i.e. the band gap is increased. Materials with a large bulk Bohr exciton radius are typically good candidates for strong quantum confinement effects in QDs. The shift in band gap from the bulk value to that of the first excitonic transition for the QD of radius R is given by [9]

$$\Delta E_g = \frac{\hbar^2 \pi^2}{2R^2} \left(\frac{1}{m_e^*} + \frac{1}{m_h^*} \right) - \frac{1.8q^2}{\epsilon R}. \tag{2.48}$$

The first term in Equation 2.48 is a modification of the particle-in-a-box energy for an infinite quantum well of width R. This can be compared to Equation 2.3 when deriving the energy states for the bulk crystal. The second term is an additional shift due to the Coulombic interaction of the exciton bound pair. As R decreases, both terms increase and the band gap shifts to larger values. This model does not hold for very small R values, as it is based on a particle in $V=0$ potential well between the infinite walls of th well. As R decreases, the discrepancy becomes significant and there is no longer a parabolic dispersion relation [10].

A more accurate model begins not from a large well and decreasing in size, but from a molecule with few atoms and building up, the general field of study being molecular orbital theory. As stated in Section 2.1, discrete atomic states split when more than one atom is clustered together. When chemically bound, the electron states of two atoms hybridize to form a bonding and anti-bonding molecular orbitals. The bonding orbital is of lower energy and is therefore initially occupied, while the anti-bonding

31

orbital remains unoccupied. As more atoms make up the molecule, these bonding and anti-bonding orbitals split in a similar way that atomic energy states split in the bulk to form energy band formation. The bonding orbitals are called highest occupied molecular orbital (HOMO) levels, while the empty anti-bonding orbitals are the lowest unoccupied molecular orbital (LUMO) levels. These act as the molecular equivalent to the valence and conduction bands in solids. The energy difference between the HOMO and LUMO is the effective band gap of the molecule. For quantum dots, with atoms numbering in the range of 10^2 to 10^5, molecular orbital theory cannot calculate exact energy states, however it does work better for smaller QD calculations in contrast to the particle-in-a-box model. Quantum dots can be considered an intermediate material between a molecule and a crystal [11].

2.6.2 Optical Properties

Quantum dot energy gaps are characterized by the prominent first peak in absorption spectra of solutions or thin films. An example is shown in Figure 2.12 for PbS. The QD-size-dependence of the peak demonstrates the tunability of the energy gap. The peak corresponds to the lowest energy electron transition. Schematically, this is shown in Figure 2.13. These quantized states sit near the band edges, however, deeper within the bands, the density of states approaches the continuity of the bulk material leading to many more possible transitions [12]. This appears as the large increase in absorption at higher energies. The labeling scheme for quantum dot is similar to that of atomic states (principle and angular quantum numbers), but arise from the spherical
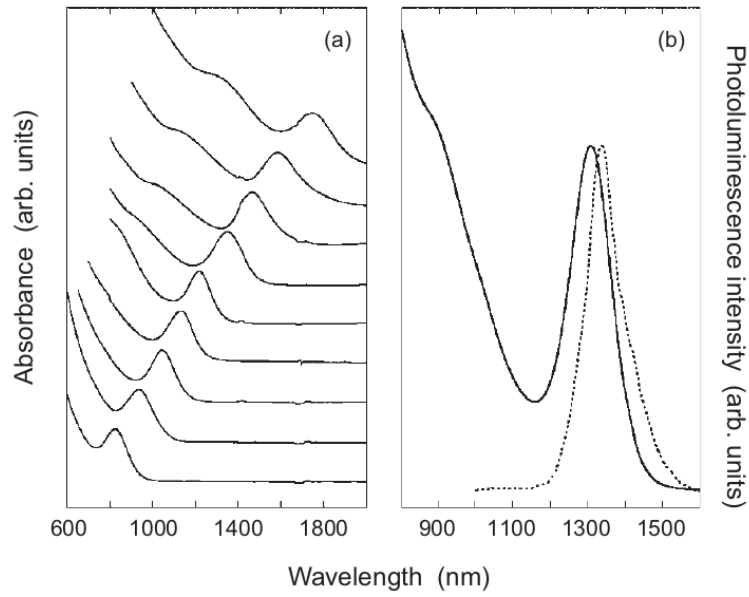
Figure 2.12: (a) Absorption spectra of different sizes of quantum dots demonstrating the size-dependence of the energy gap. (b) A sample absorption (solid) and photoluminescence spectrum (dotted).

Bessel function and spherical harmonic solutions to a particle in a spherical well [13]. The lowest energy states for electrons and holes are $1S_e$ and $1S_h$ respectively. The higher angular momentum naming scheme P, D, etc. continues for higher excited electron and hole states as well.

The tunability of QDs allows for a layered structure in solar cells, with large band gaps in front, absorbing high energy photons and allowing lower energy light through to lower levels. This grading of the bandgap allows for more efficient absorption than a single bandgap material.
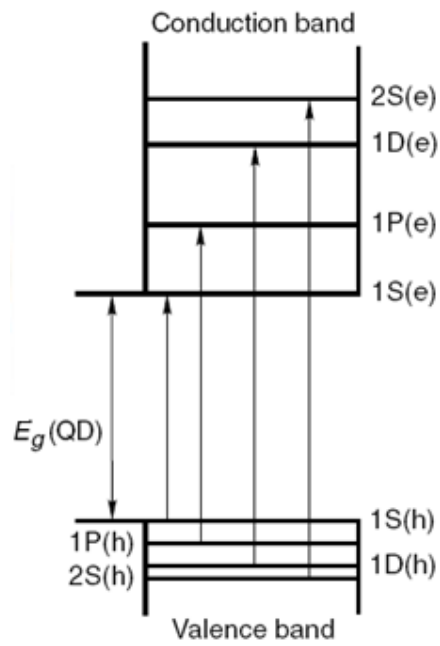
Figure 2.13: Schematic diagram depicting electronic transitions within a quantum dot. The effective bandgap energy is the energy difference between the highest hole state $1S(h)$ and lowest electron state $1S(e)$.
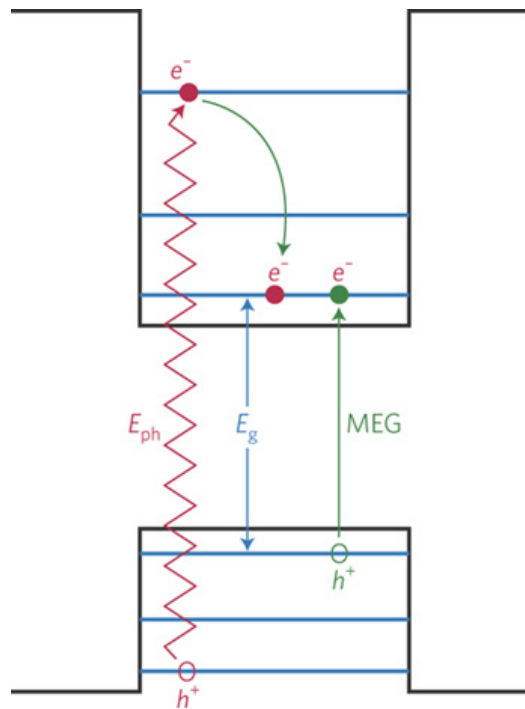
Figure 2.14: Schematic representation of the MEG process.

2.6.3 Multiple Exciton Generation

One the most attractive properties of some quantum dots is their potential to create more than one EHP for an incident photon. This is called multiple exciton generation (MEG). The process is schematically shown in Figure 2.14. A high-energy photon is absorbed, exciting an electron to a high-energy state. The electron then relaxes to the $1S_e$ QD state, transferring its energy to another electron in the valence band creating a second EHP in the process. This has been proposed as a way to break the Shockley-Queisser limit—the fundamental thermodynamic limit to single junction solar cells.

2.6.4   Surface States

Bulk semiconducting crystals have a very small surface-to-volume ratio, typically leading to surface states contributing much less to material properties than bulk states. For quantum dots, this in not the case. Being comprised of such a small number of atoms leads to $\sim15\%$ being on the surface of a quantum dot [14]. These atoms on the surface are partially bound only to inner atoms, with outer electronic bonds unsatisfied, the states of which often lie within the band gap [15]. These sites are good candidates for trapping charge carriers, affecting performance within devices.

To ameliorate this problem, surface passivation of quantum dots is required. This is a similar process used in hydrogenating amorphous silicon in thin film solar cells. For QDs, often an organic ligand is bound to the surface of the dot, passivating the bonds. The ligand also serves as a spacing agent within thin films in order to preserve the quantum separation of the dots. In addition, it could functionalize the dot for solubility within a solution [16].

2.6.5   Electron Transport Between QDs

Quantum dot charge transfer depends not only on the dots themselves, but also the properties of their environment. Often, layers of QDs are considered a super lattice of pseudo-atomic bound states. Their separation depends on the material they are embedded within. Often this is an organic-ligand network, as discussed above. To move from one QD to another, electrons must escape the binding energy of the well. This can be done through thermal excitation, classical electrical repulsion, or quantum

tunneling.

Quantum dots can be considered a quantum well. As EHPs are generated upon light absorption, the charges are separated at the QD surface. Photon-electron interactions can excite charge carriers enough to hop to neighboring QDs, eventually reaching an electrode. This thermally activated hopping mechanism can be modeled through the Frenkle-Poole emission J-V relationship given by

$$J \propto V \exp\left(\frac{A(B - \sqrt{V})}{kT}\right),$$ (2.49)

where A and B are constants.

If charge builds up within an individual QD—enough to repel additional charge—a space-charge steady state is established [17]. This limiting current is described by

$$J = \frac{9\epsilon\mu V^2}{8L^3}.$$ (2.50)

This occurs when charge builds up near one electrode that is a distance L from another, with material with dielectric constant ϵ between. μ is the carrier mobility within the material.

A charge carrier within a QD can quantum-mechanically tunnel through the surrounding material barrier into another QD leading to device current. This depends on the energetic barrier height between QDs and the distance between dots. This can

be seen in the quantum tunneling probability given by

$$|T|^2 \propto \exp{-2\kappa L}, \qquad (2.51)$$

where κ is quantum mechanical wavevector of the charge carrier:

$$\kappa = \frac{\sqrt{2mU}}{\hbar}. \qquad (2.52)$$

This tunneling probability can be modified if, instead of a flat potential barrier, the wells are separated by a tilted barrier due to an electric field. This barrier would require less energy to tunnel through since the depth varies with distance. This tunneling mechanism is called Fowler-Nordheim tunneling. Both tunneling processes lead to current given by

$$J = \frac{q\sqrt{E_f/\phi}}{4\pi^2\hbar(E_f + \phi)}\mathcal{E}^2 \exp\left(-\frac{4}{3}\frac{\sqrt{2m\phi^3}}{\hbar\mathcal{E}}\right). \qquad (2.53)$$

E_f is the Fermi energy of the semiconductor and ϕ is the workfunction of the metal.

It is worth noting that tunneling processes are temperature-independent, in theory. However, their current depends on barrier height and length. In solution-processed QD films, this depends on the capping ligand length, which, in turn, could contract and expand with varying temperature. Even though J-V equations don't explicitly demonstrate a temperature dependence, the device current could change because of material thermal properties.

Chapter 3

Semiconductor Junctions

When a p-type semiconducting material of acceptor concentration N_a is put in contact with an n-type material with donor concentration N_d, the difference in charge density on either side of the contact will cause charges to diffuse across the interface as discussed above; electrons move into the p-type region, and holes into the n-type region.

This diffusion of charge carriers is in opposition to the drift current established by the band bending that occurs due to the difference in Fermi energy levels in the two materials. If the Fermi level is different in two materials in contact with each other, charges will distribute themselves in such away to ensure that E_f is flat across the boundary. With a flat Fermi level, the valence and/or conduction band must have a non-zero gradient, leading to a built-in electric field. This is comparable to the conditions of Section 2.5 above, where the field was due to an externally applied source. Here, the difference in Fermi levels leads to a contact potential driving drift current across the boundary. These drift and diffusion currents for and electrons is shown in Figure 3.1.
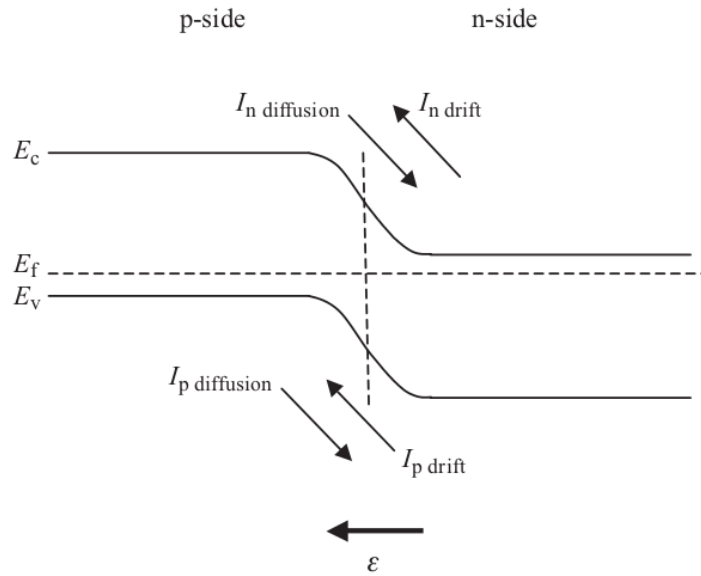
Figure 3.1: When p- and n-type materials are put in contact, energy bands bend causing the flow of charges due to drift and diffusion currents in the directions shown.

Very close to the interface, nearly all dopant atoms are ionized; electrons in the n region move to fill in acceptor sites in the p region, leaving positive stationary ions in the n region. This can also be seen as holes traveling into donor sites in the n region, leaving negative ions on the p side of the junction. The level of depletion of dopants decreases as you move away from the interface. This exists as a charge density gradient, highest the interface and decreasing into neutral material far from the interface.

The gradient of charge carriers is often simplified to the case of fully ionized donor and acceptors up to the fixed distance on either side of the interface, beyond which the material is neutral. This depletion approximation can be used to build up the build-in potential and field driving charges across the barrier from Gauss's law. From charge conservation and since the materials were neutral before placed in contact,

the number of electrons that diffuse to fill acceptor states must equal the number of holes moving into donor states. Due to the fact that the donor and acceptor number density is fixed, and assuming both materials have the same cross-sectional area, the only term that varies to meet this equality is the depletion width W_0, which is different in the n and p regions:

$$Q = qN_aW_{p0}A = qN_dW_{n0}A. \tag{3.1}$$

As before, the subscript zero indicates these are equilibrium values for depletion depths into the n and p regions.

Using Gauss's Law, which relates the charge density to the divergence of the electric field,

$$\nabla \cdot \mathcal{E} = \frac{\rho}{\epsilon_0}, \tag{3.2}$$

the constant charge density of the depletion approximation leads to a linear electric field peaked at the interface and falling to zero at either end of the depletion width where there exists zero net charge.

For the contact potential V_0, the linear electric field is integrated through the depletion region leading to the potential bands bending as discussed above:

$$
\begin{aligned}
V_0 &= -\int_{W_{p0}}^{W_{n0}} \mathcal{E} \cdot d\mathbf{x} \tag{3.3}\\
&= \frac{qN_dW_{n0}W_0}{2\epsilon\epsilon_0} \tag{3.4}\\
&= \frac{qN_aW_{p0}W_0}{2\epsilon\epsilon_0}, \tag{3.5}
\end{aligned}
$$

with the full depletion width being

$$W_0 = W_{n0} + W_{p0}. \tag{3.6}$$

Since the depletion widths in each region is related to the dopant density through Equation 3.1, the contact potential can be rewritten in terms of densities and the total width from Equation 3.6 as

$$V_0 = \frac{q}{2\epsilon\epsilon_0} \frac{N_a N_d}{N_a + N_d} W_0^2, \tag{3.7}$$

and the depletion with is therefore given by

$$W_0 = \sqrt{\frac{2\epsilon\epsilon_0 V_0}{q} \left(\frac{1}{N_a} + \frac{1}{N_d} \right)}. \tag{3.8}$$

The relation between charge density, electric field, and potential is shown in Figure 3.2.

3.1   Diode Behavior

The above discussion assumes equilibrium conditions with no applied field. This led to the drift and diffusion currents canceling out. However, independently they are non-zero and can be quite large. Surprisingly, this situation holds for both a reverse (positive voltage terminal connected to the n-type side) and also a moderate forward (positive voltage terminal connected to p-type side) bias [8]. This low-level injection situation occurs when a small amount of net charge flows across the depletion region.

42
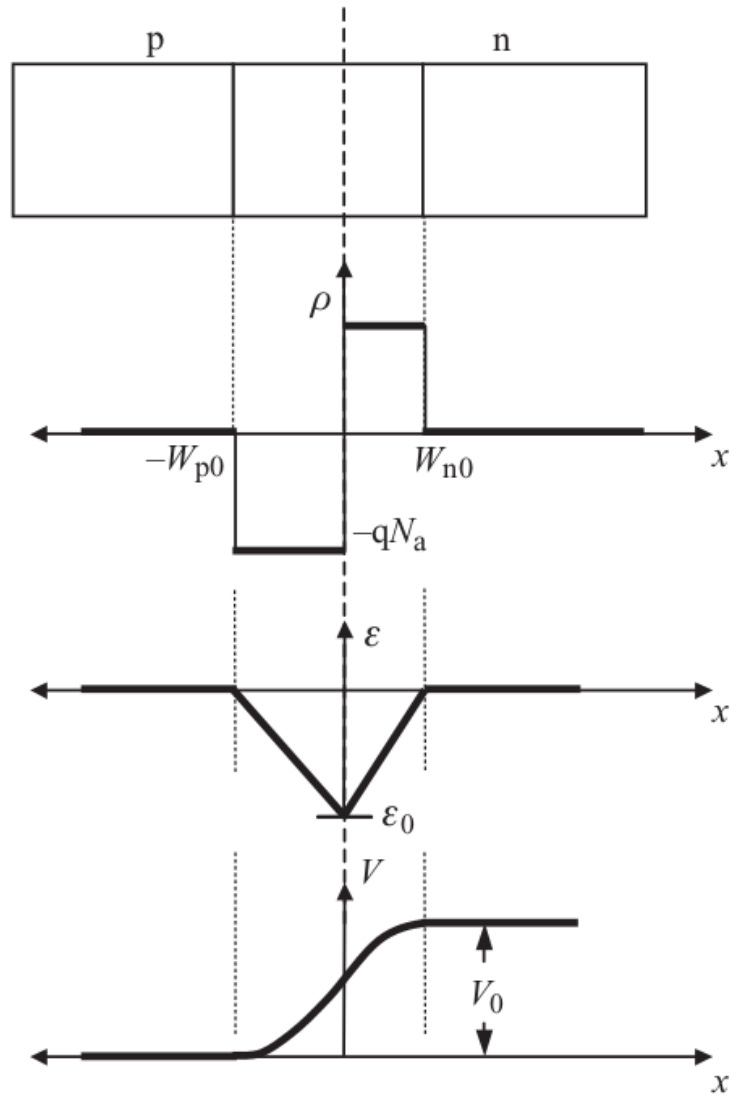
Figure 3.2: A *p-n* junction under the depletion approximation, with charge density extending to different depths on either side of the junction. The built-in electric field and potential are shown, which lead to the contact potential V_0.

When the applied bias approaches the built-in potential, a large current will suddenly begin to flow. This fast turn-on with a preferential direction gives diodes their desirable qualities for use in circuits.

There exist two types of currents—drift from electric fields, and diffusion from density gradients—for the two types of charge carriers—electrons and holes—in the two types of materials—n-type where holes are the minority carries with density p_n, and p-type where electrons are the minority carriers with density n_p. Much of the discussion of current flowing through a diode depends on the concentration of minority carriers at the boundary of the depletion regions at $x=-W_p$ and $x=W_n$, where $x=0$ is the interface between p- and n-type materials (cf. Figure 3.2). The reason for this dependence is seen by considering what happens when a reverse or small forward bias is applied. At equilibrium, the p-type region is shifted up in potential compared to the n-type in order to match Fermi levels across the junction. No current flows as discussed in Section 2.5.5. A small reverse bias causes an electric field to oppose the flow of majority carriers between the regions, but promotes the flow of *minority* carriers. Any minority carriers near the depletion edges will be swept up by the field and cross the boundary. The inherent low density of minority carriers means that this current is small, and device polarity makes this current negative. When the reverse bias is increased, the potential barrier only grows for majority carriers, but is stronger for minority carriers. No additional current flows, however, because there are not additional charges available to contribute to conduction. This constant current at negative bias is the reverse saturation current J_0. For very large reverse bias voltages, diode breakdown

44

occurs and large, negative currents can flow in response to additional negative voltages.

At forward bias, majority carriers begin to be able to flow across the depletion region due to the potential barrier being decreased. Holes from the p-type side enter the oppositely-doped material where they become minority carriers. Here, they recombine with the donor electrons with characteristic lifetimes τ_p. As the majority carriers are depleted through this process, extra charge carriers from outside the semiconductor take their places. This is the measured current flowing through the circuit.

3.1.1 Ideal Diode Equation

The dynamic equilibrium of non-zero drift and diffusion current canceling each other out leads to a density of holes at W_n being

$$p(W_n) = p_n \exp\left(\frac{qV}{kT}\right), \tag{3.9}$$

which leaves the minority carrier concentration equal to the equilibrium value when zero bias is applied, as expected, and exponentially increases a voltage increases. Similarly for electrons,

$$n(-W_p) = n_p \exp\left(\frac{qV}{kT}\right). \tag{3.10}$$

Looking at holes, this is in excess of the already-present minority carrier density p_n. Therefore, the change in minority carrier density at the depletion region boundaries

due to an applied voltage is

$$\Delta p_n = p_n \exp\left(\frac{qV}{kT}\right) - p_n = p_n \left[\exp\left(\frac{qV}{kT}\right) - 1\right]. \tag{3.11}$$

This shows that the minority carrier density at the boundary can go from nearly zero to p_n at large reverse bias, up to an exponentially large value for large positive V.

These relationships can be derived from energy levels as well. Since this is not in equilibrium, the Fermi energy cannot be used. However, the quasi-Fermi energies from Section 2.5.1 are valid. Using Equation 2.21 under the low-level injection assumptions made above ($n \sim n_0$ on the n side),

$$F_n - F_p = kT \ln\left(\frac{p}{p_n}\right), \tag{3.12}$$

which gives the change in minority carrier density due to the difference in quasi-Fermi levels as

$$\Delta p_n = p - p_n = p_n \left[\exp\left(\frac{F_n - F_p}{kT}\right) - 1\right]. \tag{3.13}$$

This is similar to Equation 3.11 given that the external bias V is what caused the quasi-Fermi levels to change, which is indeed the case. The above discussion similarly holds for electrons in the p-type region.

To relate these carrier density changes to a diode current, the diffusion equation for holes—Equation 2.42—is used with the boundary of the depletion region being $x=0$

where the density is given by Equation 3.11. Solving

$$\frac{d^2\delta p}{dx^2} = \frac{\delta p}{L_p^2} \tag{3.14}$$

again leads to exponential solutions. With this boundary condition, the change in minority carrier density is given by

$$\delta p = p_n \left[\exp\left(\frac{qV}{kT}\right) - 1 \right] \exp\left(-\frac{x_n}{L_n}\right), \tag{3.15}$$

where x_n is the distance from edge of the depletion region in the n-type material. The hole diffusion current density as a function of position is given by

$$J_p = qD_p\frac{d\delta p}{dx_n} = -\frac{qD_p}{L_p}p_n \left[\exp\left(\frac{qV}{kT}\right) - 1 \right] \exp\left(-\frac{x_n}{L_n}\right). \tag{3.16}$$

Again, similar relationships hold for electron current in the p-type material.

Further from the depletion region boundaries, the current exponential decays. This is due to more minority carriers having recombined in transit, which is also the reason for the exponential decay of excess minority carrier concentrations. The total amount of current drawn from external sources to replace the recombined majority carriers on either side of the depletion region as discussed above is given by the maximum current supplied at the boundaries of the depletion region (x_n=x_p=0). The total current

47

density flowing through diode under an applied bias V is

$$
\begin{aligned}
J &= J_p(x_n = 0) - J_n(x_p = 0) & (3.17) \\
&= q\left(\frac{D_n}{L_n}n_p + \frac{D_p}{L_p}p_n\right)\left[\exp\left(\frac{qV}{kT}\right) - 1\right] & (3.18) \\
&= J_0\left[\exp\left(\frac{qV}{kT}\right) - 1\right], & (3.19)
\end{aligned}
$$

where J_0 is the reverse saturation current described earlier. Equation 3.19 is the ideal diode equation, which ignores lossy effects such as recombination within the space-charge region and bulk resistances.

3.2   Non-Ideal Diodes

When recombination in the depletion region is taken into account, the diode equation must be modified to account for this loss in current. When forward bias is applied, excess charges are present in this depletion region. However, the majority carriers remain depleted. This combination leads to an increased chance of the transiting excess charges recombining into trap states within the depletion region. Previously this could be ignored in equilibrium because the density of majority carriers was so high they essentially filled all the traps.

Looking at the rate of recombination—not direct electron-hole recombination from E_c to E_v, but electron to traps or holes to traps, which are assumed to be deep in the gap ($E_t \approx E_g/2$) since thermal fluctuations can empty shallow traps—and ignoring

48

optical generation within the depletion region,

$$R = -\frac{d\delta p}{dt} = \frac{\Delta p}{2\tau_p},$$

(3.20)

where the extra factor of $1/2$ for the recombination rate is due to half of the traps being filled from the Fermi-Dirac distribution value at the mid-gap trap states.

The product of charge carriers are related to the quasi-Fermi energies on either side of the depletion region, which, in turn, is related to the applied bias V by

$$\delta n \delta p = n_0 p_0 \exp\left(\frac{F_n - F_p}{kT}\right) = n_i^2 \exp\left(\frac{qV}{kT}\right).$$

(3.21)

Excess electrons δn can be assumed to equal the excess holes δp if the quasi-Fermi energies are symmetric about the interface. This leads to the recombination rates being

$$R_p = \frac{n_i}{2\tau_p} \exp\left(\frac{qV}{2kT}\right)$$

(3.22)

$$R_n = \frac{n_i}{2\tau_n} \exp\left(\frac{qV}{2kT}\right).$$

(3.23)

The charges that recombine within the depletion region are replaced by external charges, which affect the measured diode current, which was shown in Equation 3.19 to go as $\exp(qV/kT)$ at forward bias. This is modified through recombination currents by adjusting the ideal diode equation to the form

$$J = J_0 \left[\exp\left(\frac{qV}{nkT}\right) - 1\right].$$

(3.24)

The factor n in the exponential is called the ideality factor, which can vary from 1 for an ideal diode to 2 for heavy recombination.

Instead of recombination in the depletion region, if excess charges are generated through optical absorption or thermal excitation of trap states, the reverse saturation current J_0 is no longer constant under reverse bias. This is due to the strong electric fields within the depletion region sweeping the excess charges towards the neutral bulk where they recombine. Thermal generation of carriers from trap states is seen as a $\sqrt{V}$ dependence of J_0 due to the depletion width dependence shown in Equation 3.8; as W expands, more traps are present in the depletion region.

3.3   Diode Interfaces

The above discussion assumed the p- and n-type material are made of the same substance having the same band gap, the difference being the doping type only. This diode is called a homojunction. Diode homojunctions can be made with opposite doping types as well as a highly-doped material in contact with a lower doping but of the type i.e. n^+-n or p^+-p junctions. These are called isotype homojunctions, in contrast to the anisotype p-n junction as assumed above.

When the two materials have different band gaps, the diode is called a heterojunction, which can also be iso- or anisotype. Both the PbS and Ge devices discussed herein are heterojunctions, with ITO being a large band gap semiconductor/insulator compared to the relatively narrow gap of the quantum dots.

50

Besides semiconductor-semiconductor interfaces, diodes can be made with semiconductors in contact with metal. The diode behavior arises from the mismatch of the metal's electron affinity and the semiconductor's conduction band, leading to selective charge separation. These contacts create Schottky diodes. The matching of electron affinity and E_c or E_v of the semiconductor leads to an Ohmic contact, which is desirable for efficient charge collection in solar cells.

3.4   Interface Transport

The transport of electrons between quantum dots was discussed in the previous chapter, with several models for electron transport provided. Much of the theory translates into device interface transport, which can be seen from the QDs' interaction being a potential barrier that must be overcome, similar to what is encountered between two different semiconductor materials.

For a heterojunction, there may be a sharp potential barrier at the interface, which may be thermally overcome or tunneled through, similar to charge transfer between QDs. For such a barrier, the current density is given by

$$J = \frac{(kT)^2 m^* q}{2\pi^2 \hbar^3} \exp\left(-\frac{qV_b}{kT}\right) \left[\exp\left(\frac{qV}{kT}\right) - 1\right], \qquad (3.25)$$

where V_b is the barrier height the charge carrier must overcome. This can be compared to the thermionic emission equation presented for QD charge transfer.

Building, again, from the QD charge transfer mechanisms discussed above, tun-

neling transport can occur by charges quantum mechanically having non-zero probability of existing in a classically-forbidden region of material. This probability is enhanced when tunneling is allowed to be a multi-step process. This tunneling starts at, say, the valence band for holes, tunneling to intermediate band states until finally reaching the conduction band where it recombines. This multistep tunneling is temperature-dependent [18] and given by

$$J = J_0 \exp(A \times V) = J_{00} \exp(\gamma \times T) \exp(A \times V), \tag{3.26}$$

where J_{00} is a constant that depends on tunneling probability and γ is the temperature dependence of the gap.

If instead of tunneling between gap states in a multi-step recombination process, the tunneling leads to a midgap trap state where the carrier is captured then emitted, th tunneling current can be modeled by [19]

$$J = J_0 \left[\exp(AV) - 1\right] = J_{00} \exp(-E_a/kT) \left[\exp(AV) - 1\right], \tag{3.27}$$

where E_a is the activation energy and A is a constant. Both tunneling processes are shown in Figure 3.3.

52
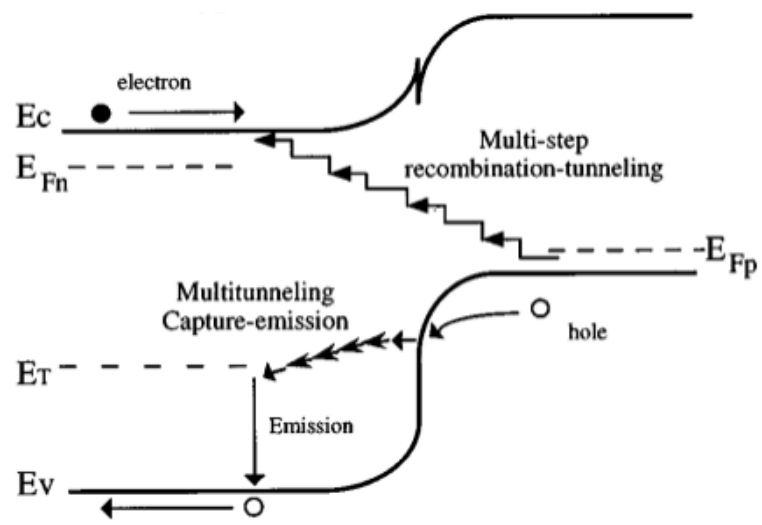
Figure 3.3: Two types of tunneling current through the device interface.

Chapter 4

Solar Cells

In moving from the properties of semiconductors and the junction devices they compose, their reaction to illumination is presented. To begin, the properties of the solar spectrum is discussed, leading to a solar cell's potential efficiency under such illumination. A non-ideal model of a photovoltaic diode is presented with methods of quantifying the ideality of devices. A brief overview of conventional solar cells commercially available leads to how QD PV cells fit into current improvements in dollars-per-watt figures.

4.1   Solar Spectra

In order to compare solar cell efficiencies, standard reference spectra of incident radiation are used. The four standards encountered in the literature are AM0, AM1.0, AM1.5D, and AM1.5G. The "AM" stands for air-mass, with the number following indicating the thickness of the atmosphere the solar radiation passes through to reach the solar cell; the higher the number is above 1, the greater the deviation from the sun
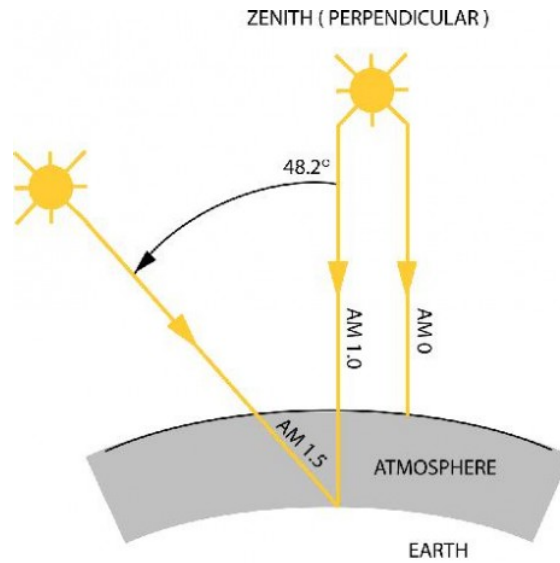
Figure 4.1: Schematic representation of path of incident sunlight for three solar spectra. The air-mass value is given by $1/\cos\theta$, where θ is the incident angle of sunlight.

being directly overhead. Figure 4.1 shows a schematic representation of the incident angle leading to these values. AM0 is the unimpeded spectrum directly from the sun. This is encountered above the earth's atmosphere and is therefore most often used for cells that are to be deployed on satellites. AM1.0 is the spectrum that reaches the earth's surface from the directly-overhead sun after passing through the atmosphere. Several wavelength bands are absorbed by constituent molecules e.g. water vapor and CO_2. The AM1.0 spectrum is the reference for cells to be used in equatorial regions.

A thickness of 1.5 times the atmosphere is taken as a general average experienced by solar installations in highly populated latitudes. AM1.5D and AM1.5G, are both what is incident after sunlight passes through this 1.5-atmosphere average. Their difference lies in the inclusion or exclusion of albedo from the surroundings. AM1.5D
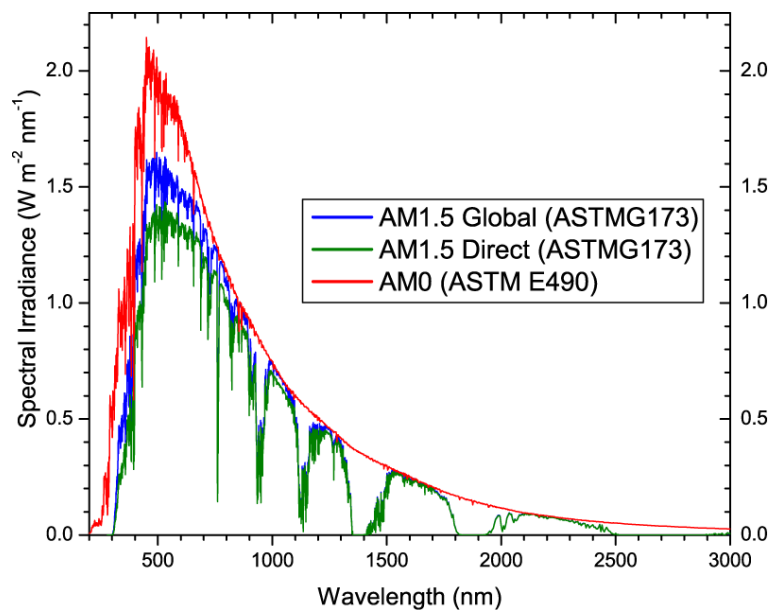
Figure 4.2: Solar irradiance of three different spectra. The deep absorption bands in the AM1.5 spectra are due to atmospheric molecules such as ozone, water vapor, or CO_2.

is the *direct* spectrum (no albedo), while AM1.5G is the *global* spectrum, including the light due to reflection off of surroundings. These two spectra are shown compared to the AM0 spectrum in Figure 4.2. For use in power conversion efficiencies, AM1.5D corresponds to 80 mW/cm^2, while AM1.5G provides 100 mW/cm^2 of radiation. This means that a kilowatt of potential solar power is incident on each square meter—a Gigawatt per square-kilometer!—under this illumination. The solar simulator used herein closely matches the AM1.5G spectrum, and therefore 100 mW/cm^2 was used in efficiency calculations.

56

4.2　An Ideal Solar Cell: The Shockley-Queisser Limit

As an introduction to the principles governing photovoltaic device operation, an overview of the Shockley-Queisser Limit calculation is presented.

In 1961, William Shockley and Hans Queisser worked out the theoretical efficiency limit of a single photovoltaic absorbing layer to be $\sim$33% [20]. The Shockley Queisser Limit (SQL) is based on the assumption that all photons with energy greater than the bandgap are absorbed and generate EHPs, which are all collected at the electrodes. If the the photon energy is greater than the band gap, the excess energy given to charge carriers is thermally exchanged until the carrier reaches the band edge. The only allowed loss mechanism is the spontaneous radiative recombination of EHPs resulting from the detailed balance calculation.

Under the above assumptions, the power conversion efficiency of a solar cell of absorbing material with energy gap E_g is given by

$$\eta = \frac{P_{out}}{P_{in}} = \frac{\max|J \times V|}{\int_{E_g}^{\infty} E\Phi_{sun}(E)dE},\tag{4.1}$$

where Φ_{sun} is the incident solar radiation flux. For the SQL, the AM1.5G standard spectrum is used.

The voltage V in Equation 4.1 is an externally applied bias, which, in the presented experiments, is swept from -1 to +1 V. In commercial installations, the voltage is held near that which provides the highest output through maximum power point tracker (MPPT) systems.

The current density J in Equation 4.1 is difference between the short-circuit current density J_{sc} and the recombination current density J_{rec}:

$$J(V) = -J_{sc} + J_{rec}(V). \qquad (4.2)$$

Current is negative at positive bias providing work done on an external load, rather than the voltage driving the solar cell as is done in a typical diode. J-V curves are plotted with the focus being on the behavior in the fourth quadrant.

Under the optimal conditions of the SQL calculation, J_{sc} is given by

$$J_{sc} = q \int_0^\infty A(E)\Phi_{inc}(E)dE, \qquad (4.3)$$

where the absorption is a unit step function at the band-gap energy,

$$A(E) = \Theta(E - E_g), \qquad (4.4)$$

and Φ_{inc} is the incident flux, which includes both solar radiation as well as photons from radiative recombination:

$$\Phi_{inc} = \Phi_{sun} + \Phi_{rad}. \qquad (4.5)$$

Combining the above equations leads to the maximum short-circuit current density for
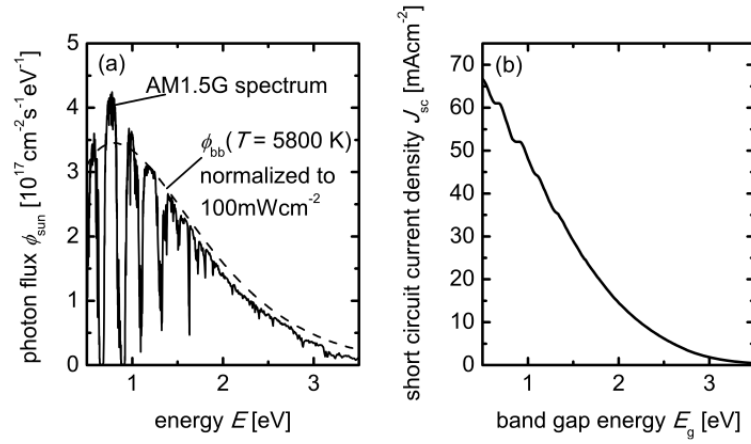
Figure 4.3: (a) The AM1.5G solar spectrum matched with a black body radiation curve of 5800 K. For this spectrum, the maximum J_{sc} is shown in (b) as a function of E_g. As E_g approaches 0, all photons are absorbed leading to maximum number of charge carriers.

a material with band gap E_g being

$$J_{sc} = q \int_{E_g}^{\infty} \Phi_{sun} + \Phi_{rad} dE. \qquad (4.6)$$

The maximum J_{sc} from Equation 4.6 is show as a function of band gap energy E_g in Figure 4.3 along side the AM1.5G solar spectrum as well as a 5800 K black body radiation curve fit to the sun.

The recombination current density J_{rec} of Equation 4.2 above is due to the loss from the radiative recombination of charge carriers in detailed balance with those generated through absorption. The emissivity is related to the radiative black body spectrum at a given temperature through the absorptance via Kirchhoff's law [21]

$$\Phi_{em} = A(E)\Phi_{rad}, \qquad (4.7)$$

59

and the recombination current density follows [22]

$$J_{rad} = q \int_0^\infty \Phi_{em} \exp\left(\frac{qV}{kT}\right) dE \qquad (4.8)$$

$$= q \int_0^\infty A(E) \Phi_{rad} \exp\left(\frac{qV}{kT}\right) dE \qquad (4.9)$$

$$= q \int_{E_g}^\infty \Phi_{rad} \exp\left(\frac{qV}{kT}\right) dE. \qquad (4.10)$$

The total current density from Equation 4.2 is then given by

$$J(V) = -J_{sc} + J_{rad} \qquad (4.11)$$

$$= -q \int_{E_g}^\infty \Phi_{sun} + \Phi_{rad} dE + q \int_{E_g}^\infty \Phi_{rad}(E) \exp\left(\frac{eV}{kT}\right) dE \qquad (4.12)$$

$$= -q \int_{E_g}^\infty \Phi_{sun} - \Phi_{rad} \left[\exp\left(\frac{qV}{kT}\right) - 1\right] dE. \qquad (4.13)$$

The term in brackets in Equation 4.13 follows the behavior of the ideal diode equation from Section 3.1. Solving for the voltage when the current is zero gives the open circuit voltage V_{oc}:

$$V_{oc} = \frac{kT}{q} \ln\left[\frac{\int_{E_g}^\infty \Phi_{sun}(E)dE}{\int_{E_g}^\infty \Phi_{rad}(E)dE} + 1\right] \qquad (4.14)$$

$$= \frac{kT}{q} \ln\left(\frac{J_{sc}}{J_0} + 1\right), \qquad (4.15)$$

where J_0 is the saturation current density, again similar to that encountered in Section 3.1.

As seen in Equation 4.6, J_{sc} decreases with increasing band gap due to few photons able to be absorbed at high E_g. However, Equation 4.15 shows an increase in V_{oc} with increasing band gap, which can be seen as the energy each charge carrier has increasing with E_g after relaxing to the band edge. This is nearly linear as shown in Figure 4.4(a) Both J_{sc} and V_{oc} are the maximum values possible for J and V in Equation 4.1 above. However, their product is what matters for PCE, therefore their values at the point of maximum power is less than J_{sc} and V_{oc}, with P peaking somewhere in between. Figure 4.4(b) shows the efficiency values of a range of band gap energies. The peak is near 1.25 eV at ∼33%, which is known as the Shockley-Queisser limit to solar cell efficiencies. It is quite remarkable that silicon—one of the most abundant elements and being relatively easily to work with, due in large part to transistor research—has a band gap of 1.1 eV—very close to the Shockley-Queisser peak. Silicon's band gap has a maximum efficiency of 29%. Breaking beyond the SQL requires modifications to their assumptions. One way is increase the intensity of incoming solar flux Φ_{sun}. This is the basis for solar concentrator systems. Another method is to use a multi-junction cell design, which stacks layers of different band gaps with blue photons absorbed at the front, allowing more red photons to pass through to deeper layers. Under 1000 suns of illuminations single junction cells can reach 37% efficiency. Double junctions can reach 50% while triple junctions can be 56% efficient under these intense conditions [23].
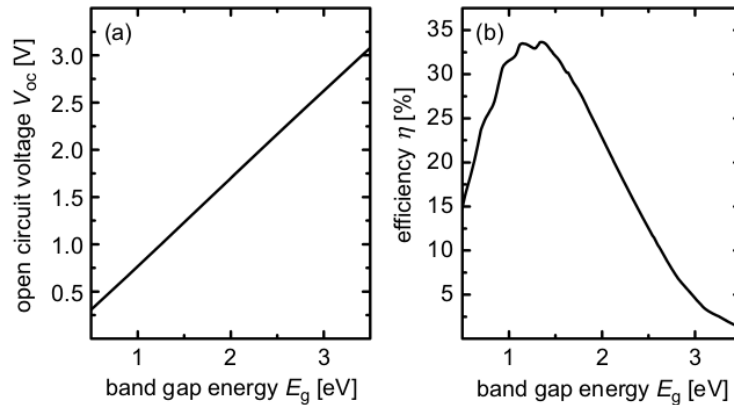
Figure 4.4: (a) The nearly linear dependence of V_{oc} on E_g is counter to the J_{sc}-E_g relationship. (b) Together, the maximum efficiency is ~33% when illuminated by AM1.5G sunlight, which corresponds to a band gap near 1.2 eV.

4.3   Non-Ideal Solar Cells

As the previous chapter discussed ideal and non-ideal diodes, this chapter moves from ideal solar cells into realistic, non-ideal behavior. This requires modifications of the diode equations (ideal: Equation 3.19, and non-ideal: Equation 3.24).

A solar cell device contains intrinsic losses arising from recombination at the *p-n* junction discussed previously, as well as extrinsic losses from poor absorption or inefficient charge collection. The exact sources of loss are difficult to characterize, however, general properties of performance are modeled by an equivalent diode circuit shown in Figure 4.5.

The equations for diode current occurs in I_D in the figure. The photogenerated current is shown as I_L an is in opposition to the diode current as discussed above with sign conventions. The total current leading to an external load I is what is left after parasitic losses through shunting pathways (I_{sh}). Any voltage drops after the diode is
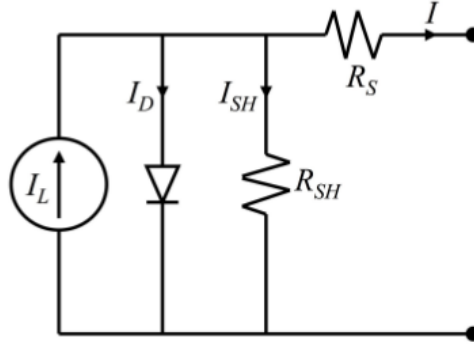
Figure 4.5: Equivalent circuit for a non-ideal solar cell.

through a series resistance R_s. For the ideal solar cell, $R_s = 0\ \Omega$ and $R_{sh} = \infty\ \Omega$.

The modified solar cell diode equation including shunt and series resistances and an intrinsically non-ideal diode is given by

$$J(V) = J_0 \left[\exp\left(\frac{q(V - JAR_s)}{nkT} \right) - 1 \right] + \frac{V - JAR_s}{R_{sh}} - J_{sc}.$$ (4.16)

A rough gauge of resistance values can be obtained from the slope of the J-V curve at V_{oc} and J_{sc}. The inverse of the slope at J_{sc} relates to R_{sh}. A flat line would be zero slope leading to infinite resistance. At V_{oc}, a vertical line would be infinite slope indicating zero series resistance. Hegedus and Shafarman [24] give a detailed description of methods for a more accurate determination of thin film device resistances as well as other diode properties.

Beyond losses and idyllic diode behavior, several figures of merit, which have already been alluded to, are used to compare devices efficacies as solar power converters. The first is the photogenerated current under zero bias. This is the short-circuit current
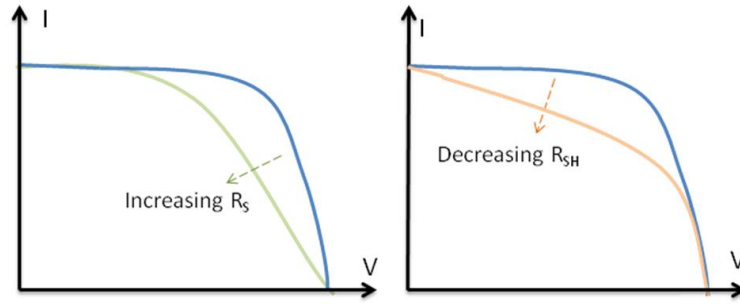
Figure 4.6: Effects of non-ideal conditions leading to poor device performance.

density J_{sc}. Under no illumination, there ideally will be no current flowing through the diode at zero bias. However, when EHPs are optically generated, the depletion region's electric field should separate the charge carriers leading to current driven through an external circuit. This additional carrier generation is a rough determinant of photo-conversion ability.

The photogenerated current is opposed to the diode current at forward bias. When the strengths of these two currents are equal and opposite, no net current will flow: $J=0$. This is the open circuit condition for a solar cell. The voltage that this occurs at is the open circuit voltage or V_{oc}.

Ideally, these two concepts combined result from the diode equation of 3.19 with a constant negative current added on, dropping the sharp turn-on of the J-V curve into the fourth quadrant. The output power is the product of the current and voltage, as indicated in Equation 4.1. The power is zero at J_{sc} and V_{oc} while nonzero in between, meaning there exists a maximum. P_{max} is found simply by multiplying I and V and seeing where it peaks. The current and voltage at this point is I_{max} and V_{max} respectively. Figure 4.7 shows the relationship between J_{sc}, V_{oc}, J_{max}, and V_{max}. The
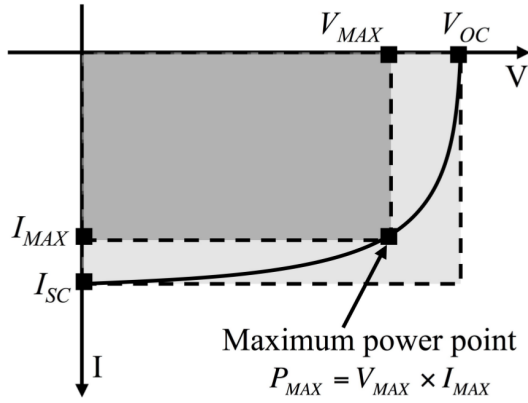
Figure 4.7: Current-voltage relationship for a solar cell under illumination demonstrating the fill factor at max power point.

maximum potential output power would be if $J_{max}=J_{sc}$ and $V_{max}=V_{oc}$. In the figure, this would be shown by the darker rectangle being the same size as the lighter rectangle. All solar cells have their max power points less than $J_{sc} \times V_{oc}$. The fraction of the larger, light gray rectangle that is filled by the darker max power point rectangle is called the fill factor (FF) given by

$$FF = \frac{J_{max}V_{max}}{J_{sc}V_{oc}}.$$

(4.17)

From Equation 4.1, this means that the solar cell efficiency is given by

$$\eta = \frac{J_{sc}V_{oc}FF}{P_{in}},$$

(4.18)

where, again, P_{in} is the radiated power incident upon the solar cell.

4.4 Photovoltaics in Practice

In 1839, at the age of 19, Alexandre Becquerel observed that an acidic solution containing silver chloride connected to platinum electrodes produced a small current when exposed to light [25]. It would be another 40 years until the first solid state PV cell was created, which was less than 1% efficient [26], and another 70 years before a more practical silicon cell was developed at Bell Labs from a p-n junction that reached 5% efficiency [27].

Today, most of the solar cells on the market are made from single-crystal silicon junction devices with potential efficiencies over 24% [28]. As discussed above, silicon is an indirect band gap material leading to weak absorption, which therefore requires larger quantities to increase the thickness of the cells. Despite silicon's high abundance, and well-established industrial processing techniques, the costs remain high. But, as the market grows, the price of PV continue to fall as seen in Figure 4.8.

Outside of market solutions to price reduction, there exist several methods to bring down the cost-per-Watt for PV. First is to use a lower quality silicon. Typical solar-grade c-Si requires a purity on the order of parts per million. This highly pure silicon is grown in cylindrical ingots and cut into circular wafers with a wire saw, leaving large amounts behind as saw dust. Polycrystalline silicon avoids some of these losses and costs by casting several crystals together in a multicrystalline ingot. These cost reduction methods come with a lower performance than the c-Si cells—around 17% [29].

Another path to lower costs is to decrease the amount of material required

66
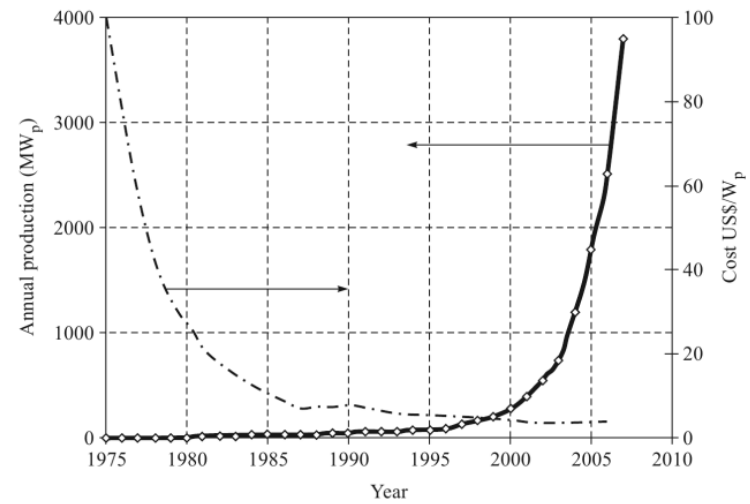
Figure 4.8: Trends in PV production mirroring that of costs over several decades.

to absorb incident radiation. This can be done through external modifications such as anti-reflective coatings or by having back reflectors redirect the light back through the material, essentially doubling the chance of a photon being absorbed by Si requiring less material to absorb the same amount of light.

When silicon is not in its crystalline structure, the band properties change. Amorphous silicon (a-Si) has a direct band gap, which increases its absorption abilities, but at a higher energy of 1.7 eV. But the short-range order leaves many unsatisfied bonds as trap sites for charge carriers, which essentially renders a-Si useless for PV devices. This can be ameliorated through the passivation of surface states with hydrogen. Hydrogenated amorphous silicon cells (a-Si:H) require as little as one micron to absorb nearly all incident light, and these films can be grown at much lower temperatures than that required for crystalline Si leading to cheaper devices. Hydrogenated amorphous silicon suffers from degradation under illumination, called the Staebler-Wronski

67

effect. The devices stabilize after an initial exposure to light, with the highest stabilized efficiency being 13.4% achieved in a triple junction amorphous cell [30].

Beyond the nearly omnipresence of silicon, several other solar cell materials are available commercially. In trying to reduce material costs, CdTe and Copper Indium Gallium Selenide (CIGS) are direct band gap materials leading to cheap, thin film devices in polycrystalline form. CdTe suffers from the toxicity of cadmium, which is banned in several countries, and low abundance of tellurium in the earth's crust. CIGS devices also suffer from the abundance issue through indium and selenium. However the much more abundant sulfur can be substituted for selenium in CIGS. The elemental abundance by weight of several solar cell constituents [31] is shown in Table 4.1.

Element	% Weight
Si	27.7
Al	8.1
P	0.1
S	0.05
Zn	0.01
Cu	0.007
Ga	0.002
Ge	0.0007
As	0.0005
Sb	0.0001
Cd	0.00002
In	0.00001
Se	0.000009
Te	0.0000002

Table 4.1: Abundance of several elements relevant to solar cell manufacturing, by weight of Earth's crust.

In addition to using cheaper materials to reduce the cost-per-watt metric,

increasing the output of the cell for the same amount of material is a attempt to reach that end. The highest efficiency single-junction cells are manufactured from gallium arsenide, which are able to reach 26.4%. Since GaAs is so expensive, they are often paired with solar concentrating optics, with lenses being cheaper than adding more solar cell area. This approach suffers from the requirement that to focus the sunlight it mush be at normal incidence onto the lens requiring much more expensive solar tracking machines. GaAs can also be improved by making multi-junction cells as discussed above. These two combined approaches have lead to the highest efficiency solar cells to date: a triple-junction GaAs device under concentration with 44% efficiency. Since these materials are so expensive, they are much lest common in terrestrial applications where their benefit of requiring less area is not so much a limit to installations. However, GaAs solar cells are often used in extraterrestrial applications where the figure of merit is pounds-per-watt since the cost of launching one pound into orbit around the earth is on the order of tens of thousands of dollars [32].

The trend of record research solar cell efficiencies for the different classes of materials is shown in Figure 4.9, which is continually updated by the National Renewable Energy Laboratory (NREL). The relatively new field of quantum dot photovoltaics is shown in the lower-right corner of the figure and is discussed in the following section.

Figure 4.9: The history of solar cell efficiency milestones. Quantum dot photovoltaics is in the bottom-right of the figure.

4.5 Quantum Dot Solar Cells

The optical properties of quantum dots were discussed in Section 2.6, which leads to their tunable absorption spectra based on QD size. The tunability of band gaps is analogous to dye-sensitized, or Grätzel, organic solar cell. This allows for potentially simple multi-junction cell fabrication. QD cells are typically solution processed, requiring much lower energy costs of fabrication. This is compared to the above materials, which exhibit bulk properties requiring bulk amounts of the material to be used in solar cells. This often means high temperatures and/or pressures in device fabrication, in addition to relatively large amounts of the material. Requiring less material and lower costs of manufacturing, together with the ease of graded bandgap layering through tuned QDs, several QD materials exhibit the potential for multiple exciton generation. This could lead to a much cheaper method of breaking the Shockley-Queisser limit than expensive concentrators or bulk multi-junction fabrication.

4.5.1 PbS Quantum Dot PV

In bulk, PbS has a band gap of 0.41 eV. This can be tuned across the optical spectrum as showed in Figure 2.12. The high tunability is due to the large Bohr exciton radius of ~18 nm. The empirical relationship between QD diameter and first absorption peak energy is [33]

$$E = 0.41 + (0.0252d^2 + 0.283d)^{-1}. \tag{4.19}$$

71

The first report of colloidal quantum dot solar cells was made in 2005 [34], with improvements to device efficiency pushing to 7% in 2012 [35]. The first devices with more than 1% PCE were Schottky cells [36–38], with ITO as the front contact and aluminum forming the Schottky barrier to facilitate charge separation. PbS Schottky devices have been able to reach 4.6% efficiency [39].

Beyond the Schottky devices, researchers presented working depleted heterojunction devices in 2010 [40], which improved upon charge separation. The following year, band gap tuning was implemented in a tandem cell with two layers of different sized QDs [41]—2 nm for visible light and 4 nm for IR—providing proof of concept for quantum tuning of a graded band gap device. With the current state of single-junction devices being 7% efficiency, further improvements are required before the possibility of a multijunction cell with greater than 15% PCE is reached [42]. The Schottky and heterojunction device schematics and band diagrams [43] are shown in Figure 4.10.

4.5.2 Germanium Quantum Dot PV

Germanium QD solar cells have not been fully realized outside of this lab as of writing. One problem with Ge (and all Group IV elements) is the strong covalent bonds requiring high temperatures to form crystals, compared to the II-VI and IV-VI QDs of e.g. CdTe and PbS [44]. In the present research, this is overcome through microwave synthesis of Ge ionic solutions, which have a larger absorption of microwaves and high photon-phonon interaction [45].

As with CdTe, a drawback to PbS devices is the toxicity of constituent ma-
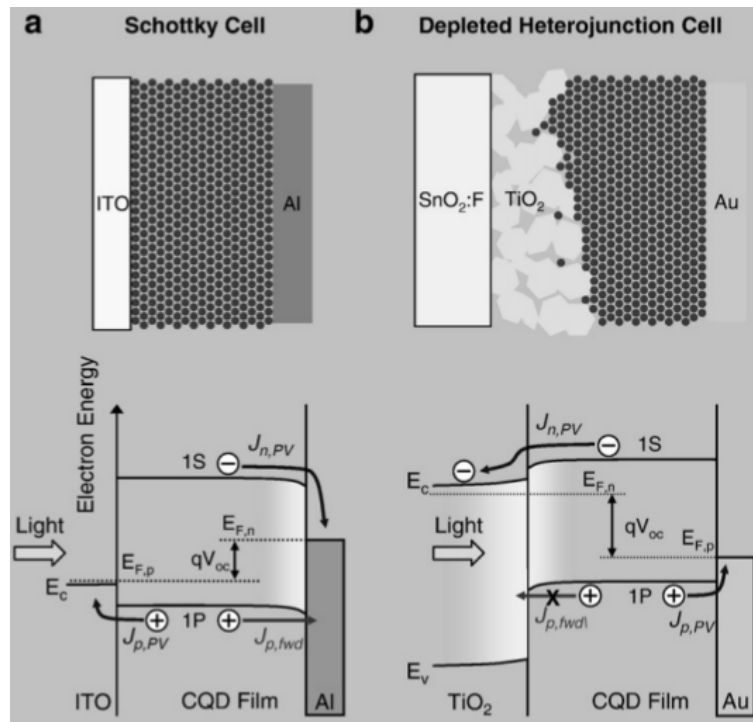
Figure 4.10: Layering schematic and energy band diagrams for a Schottky and heterojunction PbS PV device.
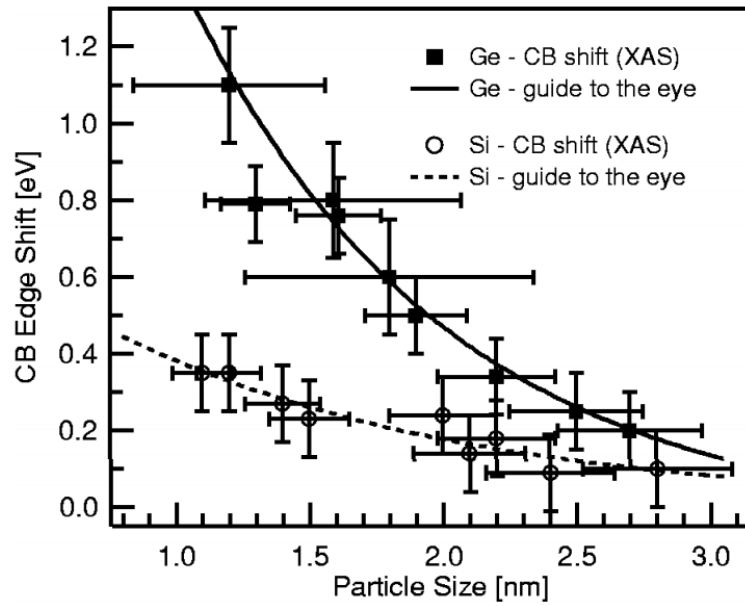
Figure 4.11: The tunability of Ge and Si absorption peak with quantum dot size.

terials, namely lead. This leads to a desire for the less toxic Group IV elements such as Si and Ge for QD PV. Compared to silicon, Ge should be a better candidate due to its more direct band gap (cf. Figure 2.1) and larger Bohr exciton radius leading to a highly tunable band gap [46] as seen in Figure 4.11.

Chapter 5

Methods

This chapter steps through the device fabrication process, leading to the working PV devices studied herein. In addition, the process of studying electronic properties will be laid out, both room-temperature, and while in the cryostat.

5.1   Device Preparation

The device structure is a layered one, starting with a 1" by 1" glass slide, which we receive pre-patterned with our front contact: a 150 nm layer of 10 mol.% tin oxide in indium oxide (indium tin oxide, or ITO). The pattern allows for six 1 mm by 3 mm devices fabricated on each slide. ITO is highly transparent (88% at 550 nm) with high conductivity—precisely what is required for a window layer of a PV device.

The ITO layer is jagged at the nanometer scale, with spikes pointing out from the smooth glass, which may lead to shorts within the thin-film devices. A buffer layer is therefore added to prevent the conducting layer from penetrating through the device.

The buffer is a layer of TiO_x sol-gel, applied before the solution of TiO_2 nanoparticles.

To prepare the sol-gel, 375 μL of titanium ethoxide— $Ti(OCH_2CH_3)_4$—is added drop-wise into a highly acidic (pH < 1) solution of 5 mL ethyl alcohol, 125 μL milli-Q water, and two drops of hydrochloric acid. The solution is capped with nitrogen gas, sealed, and left to stir for at least 24 hours before use. The drop-wise addition of titanium ethoxide ensures that TiO_2 crystals do not precipitate out of the solution, instead leaving a transparent sol-gel for our PV device applications.

The sol-gel precursor is applied to the ITO-printed slides via spin casting 40 μL at 1300 RPM, ensuring excess sol-gel is removed using ethanol-soaked cotton swabs along the slide edges after spin cycle has finished. A final, dry cotton swab may be used to ensure slide edges and back are fully clean. The sol-gel is then sintered to strengthen the glassy conductive layer. Sintering begins with one hour on a 115°C hot plate, followed by 30 minutes in a 450°C tube furnace. The resulting hardened surface is the substrate for the subsequent TiO_2 nanoparticle layer.

A layer of TiO_2 nanoparticles $\sim$37 nm in size is used as the electron collector in our PV devices. The nanoparticle solution of TiO_2 in water and ethanol is purchased from Solaronix. Again, 40 μL is spin cast, but at the slightly higher speed of 1500 RPM, followed by the same sintering treatment. This turns the milky solution into a transparent layer for light to reach the absorber.

5.1.1 PbS Device Fabrication

PbS nanoparticles are in a colloidal solution of hexane and chlorobenzene before being added to our devices. There are two methods of application: spin coating and dipping. Both processes are performed in a nitrogen glovebox, as PbS quantum dots are susceptible to air and water contamination. The spin coat process is done by dropping $\sim$40 μL of CQD solution onto the TiO_2 layers while the slide spins for 30 seconds. After each spin is finished, most of the moisture is evaporated off leaving the PbS quantum dots. A clean cotton swab removes excess material from the edges as before. This layering is repeated several times building up $\sim$150 nm of the absorbing layer of PbS QDs.

For dip coating, a less dense colloidal solution is used. The slides are dipped in PbS immediately followed by the ligand exchange solution. This is either 1,2-ethanedithiol (EDT), 3-mercaptopropanoic acid (MPA), or 1,4-benzenedithiol (BDT) solutions. Each dip is <1 second, after which the slide is allowed to dry as before, again removing excess solution from the edges. After six dipping layers, rotating the slide each time to ensure an isotropic thickness, the slide is ready for the final back electrode layer to be added.

The hole collector on our devices is a thin $\sim$100 nm layer of gold that is evaporated under high vacuum at a rate of 2 Å/s. Four devices are completed simultaneously, with each device able to begin testing right away.

Devices are stored in a nitrogen-environment glovebox as long-term air ex-

posure degrades device performance quickly, although brief (<5 minutes) exposure to ambient air has shown to slightly improve performance.

5.1.2 Ge Device Fabrication

Ge devices largely follow the same procedures as for the PbS devices. These are non-optimized, leaving room for improved performance.

The nanoparticles are synthesized in a solution of GeI_2 and GeI_4 in olylamine, which is heated via microwaves [45]. The iodides are strong microwave absorbers leading to effective heating, while olylamine bonds with the Ge^{2+} and Ge^{4+} ions capping the nanoparticles. The larger the Ge^{4+}/Ge^{2+} ratio is, the larger the nanoparticle, leading to simple size control of quantum dots. Olylamine is far too large to facilitate efficient charge transfer and a ligand exchange is performed on films used in PV devices. The shorter hydrazine ligand leads to the working devices presented herein.

Besides the absorbing layer changing, the back metal contact is aluminum instead of the gold used in PbS devices. This was chosen for good Ohmic qualities, with the Al workfunction matching well to the HOMO level for efficient hole extraction.

5.2 Temperature Variations

To expand our understanding of the way in which electrons transport through our devices, current-voltage measurements are carried out under a range of temperatures. Our cryogen is liquid nitrogen, which enabled us to reach temperatures in our

cryostat below 100 K.[1] There are two methods of sweeping the sample's temperature: one is to actively heat the device using the ITC Temperature Controller's resistive heater, the other is to allow the cryostat to warm passively to room temperature. The latter was necessary to minimize outside air contamination within the cryostat; as the liquid nitrogen boiled into gas the over-pressure kept oxygen and water from entering. Currently, the cryostat's sample mount is affixed with Tygon tubing from a nitrogen Dewar, which continually flows nitrogen gas over the sample. A drawback to this approach is that the N_2 gas is warmer than the liquid but cooler than room temperature, which means more aggressive thermal control is needed at the extremes of our temperature range.

With a safe nitrogen gas environment for the devices, resistive heating elements warm the sample, while cryogenic gas cools. Before entering the cryostat, however, the devices are exposed to air when transferring from the glovebox. This results in approximately five minutes of exposure. For PbS devices, this much exposure was shown to slightly improve device performance [47]. The samples are affixed to the cryostat's sample holder via copper wire contacts with each metal electrode on the slide. In the cryostat, a xenon light bulb is placed adjacent to the sample, which is a large source of heat during J-V measurements. This can result in $\sim$5 K increase in temperature during the -1 to 1 V sweeps. All recorded temperatures are the starting temperature of the voltage sweep. The final temperature and temperature difference are included in raw data collected by the IGOR program used.

---

[1]Liquid nitrogen boils at 77 K, but our devices sit above the liquid level, and imperfect thermal isolation raises the sample's environment above this temperature.

To prepare the cryostat for use, the outer chamber is vacuumed for 2 hours to approximately 50 mbar. This ensures a strong thermal isolation for the device while in the cryostat. The Oxford Maglab cryostat was originally intended for use with liquid helium to cool a superconducting magnet as well as samples, but the magnet is no longer operational. The liquid nitrogen is held in the helium section within the cryostat to allow for cryogenic nitrogen to enter the central sample chamber for cooling. Typically, helium would be buffered from the outside by a layer of nitrogen, but this chamber remains empty.

All electrical connections to the sample are made through the sample probe which is inserted into the top of the cryostat. This includes device contacts 1 through 6, the ITO back contact, the RTD temperature sensor, and the light source power cables. The resistive temperature detector (RTD) is a calibrated piece of manganin whose resistance is a known function of temperature. This is connected to a Keithley 2001 multimeter which outputs the sample temperature. The RTD is necessary as the ITC 503 temperature monitor is spatially isolated from the sample to where there may be up to a 40 K discrepancy in sample and cryostat temperature. Temperature settings are given to the ITC 503 and a conversion must be made to ensure appropriate ranges for sample temperature are met.

Typically, 5 K intervals of temperature are what separate each current-voltage curve, with each step pre-programmed through a custom IGOR code. The ITC can range from 77 K up to 400 K, however the sample's temperature only reach from 100 K up to ∼360 K. An additional hindrance on usable temperature ranges is the calibration

of the light source. The xenon bulb's spectrum is significantly more red than an AM1.5 spectrum and this changes with bulb temperature. Below 150 K, the spectrum is no longer considered usable as the input photon energy diverges significantly from the calibrated bulb intensity at room temperature to where the J-V data is not comparable. Therefore, sample temperature ranges from 150 K to 360 K.

5.3   Capacitance-Voltage Measurements

One oft-used method of determining several device properties, including the built-in potential, doping density, and depletion width, is capacitance-voltage or Mott-Schottky measurements [48].

A simple picture of the capacitance of a semiconductor junction is the depletion region's width W being voltage-dependent. From a parallel-plate capacitor analogy

$$C = \frac{\epsilon \epsilon_0 A}{W},$$ (5.1)

with ϵ being the dielectric constant of the material within the parallel plates, A the area of the plates that are separated by a distance W. Within a semiconductor junction, applying a reverse-bias to the device, charge is separated and builds up at opposite ends of the space-charge region, effectively creating two parallel plates of charge with dielectric ϵ between them. To measure the capacitance a small AC source is applied on top of a DC voltage which is swept through a range of voltages. The frequency response of the impedance is measured, ideally providing the capacitance of the space-charge

region. The DC-voltage-dependence of the capacitance via the depletion width leads to a value for the charge carrier density as explained below.

To begin, a Schottky diode is considered, made from a p-type semiconductor with a doping density N_a, in contact with a metal. The diode is connected to a DC voltage V with a small AC signal. When the AC voltage increases a small amount of charge dQ builds up on the metal contact of the Schottky device. This charge originated from the semiconductor and is given by

$$dQ = qAN_a dW, \tag{5.2}$$

which leads to a small increase in the depletion width dW. Plugging this into the fundamental definition of capacitance gives

$$C = \frac{dQ}{dV} = qAN_a \frac{dW}{dV}, \tag{5.3}$$

which assumes the doping density is constant over the distance dW. Solving for the charge density at the space-charge region edge leads to

$$N_a = \frac{C}{qA\frac{dW}{dV}}. \tag{5.4}$$

Differentiation Equation 5.1 with respect to voltage

$$\frac{dC}{dV} = \epsilon\epsilon_0 A \left(-\frac{1}{W^2}\frac{dW}{dV} \right), \tag{5.5}$$

and solving for dW/dV gives

$$\frac{dW}{dV} = -\frac{W^2}{\epsilon\epsilon_0 A}\frac{dC}{dV} = -\frac{\epsilon\epsilon_0 A}{C^2}\frac{dC}{dV}, \tag{5.6}$$

where Equation 5.1 was rearranged to write W in terms of C. Plugging this into Equation 5.4,

$$N_a = -\frac{C^3}{q\epsilon\epsilon_0 A^2}\frac{1}{\frac{dC}{dV}}, \tag{5.7}$$

and using the relationship

$$\frac{d}{dV}\left(\frac{1}{C^2}\right) = -2\frac{1}{C^3}\frac{dC}{dV}, \tag{5.8}$$

the charge density is finally given by

$$N_a = \frac{2}{q\epsilon\epsilon_0 A^2}\frac{1}{\frac{d(1/C^2)}{dV}}. \tag{5.9}$$

To use this relationship, the capacitance is measured as a function of DC voltage and plotted on Mott-Schottky plot showing $1/C^2$ versus voltage. This should yield a linear relationship with the slope to be used in Equation 5.9 above. This, along with the dielectric constant and cross-sectional area between the electrodes will provide the charge density of the material. Due to the area dependence of this relationship, the device area should be known to a high degree of accuracy lest the error in the carrier concentration becomes significant.

In addition to charge density, information about the potential barriers within

the device can be extracted when the depletion width Equation 3.8 is used with the capacitance given in Equation 5.1 with the bias voltage added to the contact potential V_0. To extract information from the Mott-Shottky plot described above, the capacitance/voltage relationship is written

$$\frac{1}{C^2} = \frac{2(V + V_b)}{q\epsilon\epsilon_0 N(W)}. \qquad (5.10)$$

The contact potential V_0 is changed to diffusion voltage barrier V_b, which differ by the Fermi energy: $qV_0 - qV_b = E_f$. Typically, in c-Si devices, E_f is small enough that the built-in potential and voltage barrier are approximately equal. For thin-film devices, however, this is not the case as they my differ by as much as 0.8 V [24]. The linear $1/C^2$-V dependence of the Mott-Shottky plot will intercept at the diffusion potential rather than the built-in potential as typically cited.

This derivation began by assuming a Shottky diode, which allowed for the depletion width to exist only within the p-type semiconductor. This assumption is nearly valid for p^+-n and n^+-p junctions as well, where charge conservation requires a negligible extent of the space-charge region into the heavily doped side. For nearly equal doping of p-n diodes, modifications must be made, but these are generally unreliable [48]. For an n-type semiconductor, the slope will change sign as does the reverse bias voltage polarity, though the derivation similarly holds. It was also assumed that space-charge region is fully depleted and all acceptor atoms are fully ionized.

5.4 Current-Voltage Characterization

Device behavior is characterized under dark and illuminated conditions across a range of temperatures as discussed above. The illuminated data provides PV figures of merit (J_{sc}, V_{oc}, FF, PCE R_s, and R_{sh}). Their response to temperature can elucidate information regarding energy or conduction processes. The open-circuit voltage is that required to drive the diode current against the photocurrent. Therefore, an understanding of the dark current conduction mechanism could lead to improved V_{oc} and device efficiencies.

In the dark, PV cells are non-ideal diodes. Revisiting the non-ideal diode equation, the current-voltage relationship may be written as

$$J(V) = J_0 \left[\exp(A \times V) - 1\right], \tag{5.11}$$

where J_0 is the reverse saturation current discussed earlier, and A is an exponential pre-factor, which is related to the ideality factor n. Both J_0 and A may be dependent upon temperature with the way in which they vary providing information on dominant conduction mechanism of the device [49].

The reverse saturation is of the form

$$J_0 = J_{00} \exp\left(-\frac{qV_b}{nkT}\right), \tag{5.12}$$

where V_b is the barrier height and n is 2 for recombination within the depletion region
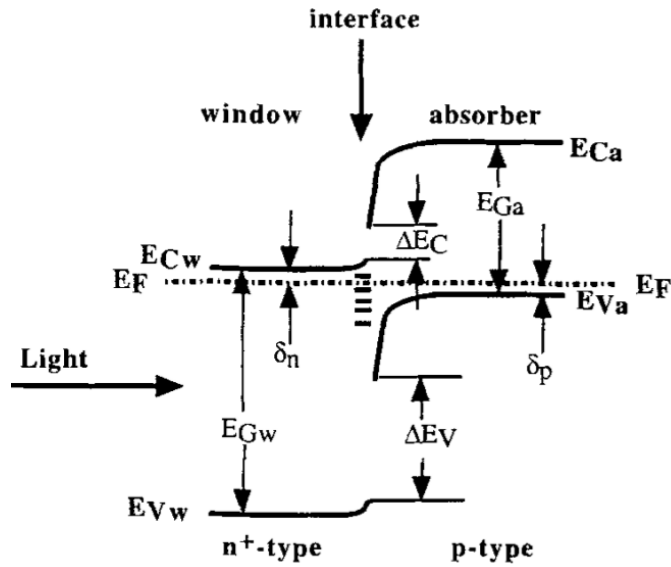
Figure 5.1: An example of a *p-n* hetero junction with *p*-type absorber layer. The band bending results from the difference in doping concentrations leading to steep barrier heights, which help prevent minority carrier recombination.

or 1 for tunneling or thermionic emission dominating conduction [50]. Figure 5.1 is an example *p-n* heterojunction similar to that of the QD cells studied herein. The barrier height for holes in the *p*-type absorber layer to reach the conduction band of the window layer is due to band bending resulting from the heavily doped *n*-type material. In this example qV_b is equal to $E_{Ga} - \delta p - \delta n - \Delta E_C$.

The exponential prefactor A may vary with temperature as well as J_0. If $A \sim q/nkT$ with $n=1$ thermionic emission is likely the dominant charge carrier due to the Boltzmann-like dependence on carrier generation. Thermionic emission conduction is characterized by $J_{00}=A^{**}T^2$ where A^{**} is the effective Richardson constant [51]. If n is between 1 and 2, it is likely that recombination within the depletion region is dominating charge transport as discussed in the non-ideal diode section above. Lastly, instead of

86

a modified Boltzmann exponential dependence, A can be independent of temperature which indicates that charges are tunneling through the barrier. The different models for charge transport and their parametric variations are shown in Table 5.1.

Conduction Mech.	J_0	A	n
Recombination	$\exp(-qV_b/2kT)$	q/nkT	≤ 2
Tunneling	$\exp(-qV_b/kT)$	Const.	$\neq$Const.
Thermionic Emission	$\exp(-qV_b/kT)$	q/kT	1

Table 5.1: Diode equation parameter variation with temperature.

The above concerns diode behavior not including photovoltaic performance. To understand the solar cell properties, looking at devices while illuminated at various temperatures provides further analytical techniques.

The total current of a solar cell under illumination is given by the difference between dark diode current and light-generated current:

$$J(V) = J_D - J_L \tag{5.13}$$

$$= J_0 \left[\exp\left(\frac{qV}{nkT}\right) - 1 \right] - J_L \tag{5.14}$$

$$= J_{00} \exp\left(-\frac{qV_b}{nkT}\right) \left[\exp\left(\frac{qV}{nkT}\right) - 1 \right] - J_L. \tag{5.15}$$

The open-circuit voltage V_{oc} is V required for no current to flow. This is often much greater than the thermal voltage and therefore the 1 in the diode equation can be ignored. Solving for V at $J=0$ provided the photocurrent is voltage-independent, meaning

$J_L = J_{sc}$,

$$V_{oc} = V_b - \frac{nkT}{q} \ln\left(\frac{J_{00}}{J_{sc}}\right). \tag{5.16}$$

This is a convenient way to obtain the potential barrier V_b faced by charge carriers in a device. Measuring V_{oc} at a range of temperatures should yield a linear curve that can be extrapolated to $T=0$K providing the built in potential barrier. Often, this energy barrier is called the activation energy E_a, which includes other possibilities for recombination e.g. in the bulk where $E_a = E_g$ [21].

There are several ways to extract the ideality factor n from J-V data. From dark curves, a fit should yield n under optimal conditions, but a more accurate way is to look at V_{oc}. It would seem from Equation 5.16 that the ideality factor can be extracted from the slope of $V_{oc}(T)$, however a better method to achieve this is to look at V_{oc} as a function of illumination intensity [52]. A semi-log plot of V_{oc} versus incident power should be linear with the slope being n times the thermal voltage kT/q. This can be seen in Equation 5.16 from J_{sc} approximately being equal to J_L, the light-induced current density, which is proportional to the light intensity as described in Section 4.2.

5.5 Nanoparticle Surface Passivation

Bare nanoparticles have a large surface-to-volume ratio, leaving a significant fraction of bonds dissatisfied. These act as trap states for charge carriers leading to poor device performance. In order to remedy this, nanoparticles are capped with molecules leading to stable, satisfied bonds. The choice of molecule clearly depends on its abil-

ity to bond to the surface, but also beneficial functionalization properties can lead to one choice being valued over others. For example, PbS QDs, when synthesized in the hexane/chlorobenzene solution, are capped with oleic acid—a long hydrocarbon chain, which is used to prevent the dots from congealing and losing their quantum isolation properties while remaining colloidally suspended within the solution. However, for device operation, the oleic acid ligand is too long to facilitate charge transport upon absorption. The molecule is therefore exchanged for a shorter capping or linker ligand.

In the presented PbS research, three different ligands are examined: 1,2-ethanedithiol (EDT), 3-mercaptopropanoic acid (MPA), and 1,4-benzenedithiol (BDT). EDT and BDT have thiol groups on either end of the chain, which could bond to two QDs making it a potential linker ligand, however MPA, with only one thiol group, is solely a capping ligand.

As discussed above, the tunneling rate for a fixed barrier is not temperature-dependent. However, if the barrier width decrease, the probability of tunneling should increase. Previous results on PbS QD PV devices demonstrated a dramatic increase in J_{sc} upon cooling the devices through the freezing point of the capping ligand [53]. This was explained through the ligand contraction decreasing QD separation distances leading to a smaller tunneling barrier. Figure 5.2 shows these previous results. By changing the choice of ligand, a change in J_{sc} temperature variation should be observed. The three capping ligands are shown with their melting temperatures in Table 5.2 along with those used in Ge devices.

In Ge QD devices, the thiol bond is too weak to facilitate passivation. N-
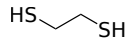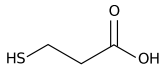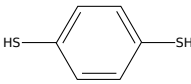
89
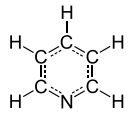
Ligand	Melting Point (K)	Structure
1,2-Ethanedithiol (EDT)	232	
3-Mercaptopropanoic Acid (MPA)	291	
1,4-Benzenedithiol (BDT)	370	
Hydrazine	275	
Pyridine	232	

Table 5.2: Melting points and chemical structures of capping ligands used in QD PV devices.

Ge bonds, however, are stable in solution and amine ligands are used in devices. A drawback is the hazardous nature of the capping ligand best suited for performance: hydrazine, which is essentially rocket fuel. Pyridine ligands have also been proposed but so far lead to poor performance.

The nanoparticles are synthesized in a solution of GeI_2 and GeI_4 in olylamine, which is heated via microwaves [45]. The iodides are strong microwave absorbers leading to effective heating, while olylamine bonds with the Ge^{2+} and Ge^{4+} ions capping the nanoparticles. The larger the Ge^{4+}/Ge^{2+} ratio is, the larger the nanoparticle, leading to simple size control of quantum dots. Again, olylamine is far too large to facilitate efficient charge transfer and a ligand exchange is performed on films used in PV devices.
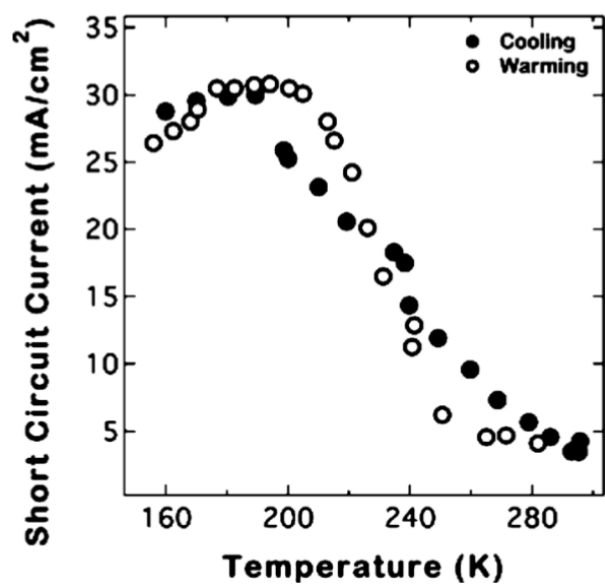
Figure 5.2: Short-circuit current density of PbS PV device demonstrating a sharp rise near the freezing temperature of the EDT capping ligand.

Chapter 6

PbS Quantum Dot Photovoltaic Devices

6.1   Introduction

Thin-film quantum dot (QD) photovoltaics provide the potential to create high-efficiency devices while simultaneously achieving a low manufacturing cost due to reduced material costs and less expensive processing. The observation of multiple-exciton generation observed in PbS QD solutions at room temperature [54] motivates further research into such devices. Although much effort is focused on improving device performance through overall structure and QD properties, relatively few studies probe the effects of temperature or capping ligands on the photovoltaic (PV) parameters [55–58]. In solid-state applications, ligands are chosen to cap QDs based on their ability to effectively transfer energy within nanostructures as well as preventing the aggregation of nanoparticles. Thiols with short chains have demonstrated both properties, making them ideal candidates for use in PV devices [59]. Previous results show that cooling the

PbS QD devices through the melting point of the ligand improves performance greatly through a six-fold increase in short-circuit current density (J_{sc}) at low temperatures [53]. This was attributed to the contraction of ligands, which increased the coupling between QDs, allowing for higher current densities. In addition to the ligands' thermal response within devices, the current-voltage-temperature parameter space reveals information regarding charge transport mechanisms.

Here, we present the effects of varying temperatures with three ligands used in PbS QD photovoltaic devices: 1,2-ethanedithiol (EDT), 3-mercapopropionic acid (MPA) and 1,4-benzenedithiol (BDT), by analyzing current density-voltage (J-V) curves in dark and illuminated conditions. EDT, MPA and BDT were chosen based on their widely varying melting points (232 K, 291 K and 370 K, respectively) and their comparatively higher open circuit voltage and short circuit currents compared to longer chain ligands. We show that the increase in J_{sc} occurs upon cooling and varies with the choice of capping ligand. In addition, MPA devices exhibit dramatically different thermal responses, as seen in the fill factor (FF) and shunt resistance (R_{sh}) data.

6.2   Methods

The lead sulfide (PbS) quantum dots (QDs) were provided by Solexant and the titanium oxide (TiO_2) nanoparticles were purchased from Solaronix. The fabrication process follows the procedure published elsewhere [53] with the device structure shown in the inset of Figure 6.1. All devices use 3.9 nm-diameter PbS quantum dots,

which correspond to an exciton peak of 1003 nm and an optical energy gap of 1.24 eV. Before the dipping process, the PbS QDs are submerged in a solution of chloroform and hexane with oleic acid as the capping ligand. The ligand exchange replaces oleic acid with the shorter ligands of EDT, MPA, or BDT for use in the devices (cf. Figure 6.2 inset). Current density-voltage (J-V) curves were taken from -1 to +1 V at varying temperatures in an Oxford cryostat with a Keithley 2400 source meter used a xenon light bulb next to the devices as the light source. The Xe bulb was chosen because it came closest to matching the solar spectrum in the region of interest (1000 nm to 400 nm) and exhibited no changes in intensity with temperature over the temperature region used in this study. The intensity was adjusted to match the J_{sc} of a commercial Si device under AM1.5, 100-mW/cm^2 illumination. After being fabricated in the nitrogen environment of the glove box, the devices were exposed to air for approximately five minutes while being transferred into the cryostat. Previous results show that this length of air exposure has a slightly positive effect on overall device performance [47]. While in the cryostat, nitrogen gas flowed across the devices. A RTD sensor placed next to the sample recorded the device temperature. Samples are warmed from the lowest temperature at a rate of ~15 K/hr, followed by cooling at the same rate. For clarity, only cooling data is shown, with no appreciable hysteresis existing between cooling and warming data.

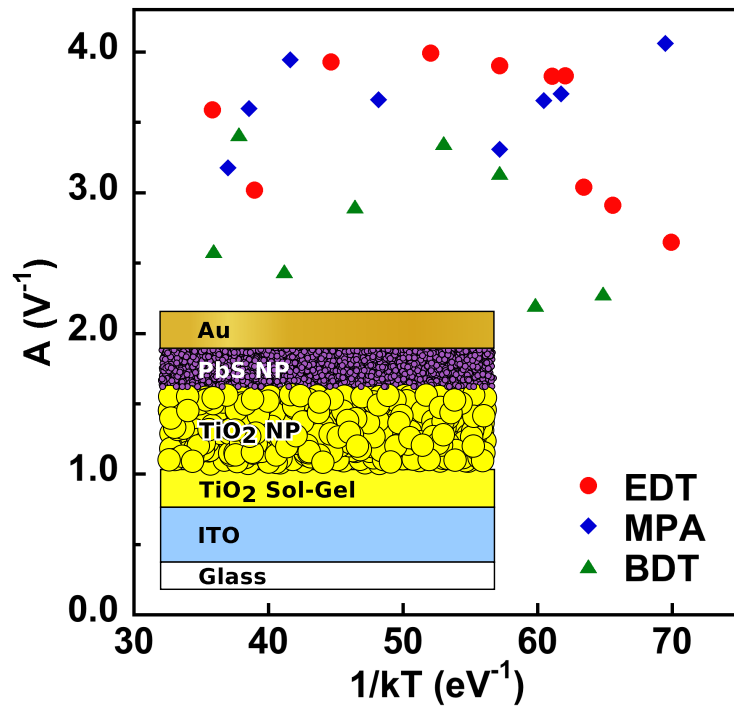Figure 6.1: The exponential pre-factor of each ligand device obtained through fitting Eq. 6.1 to dark current-voltage data taken at different temperatures. Inset: Schematic of the TiO$_2$/PbS solar cell structure.
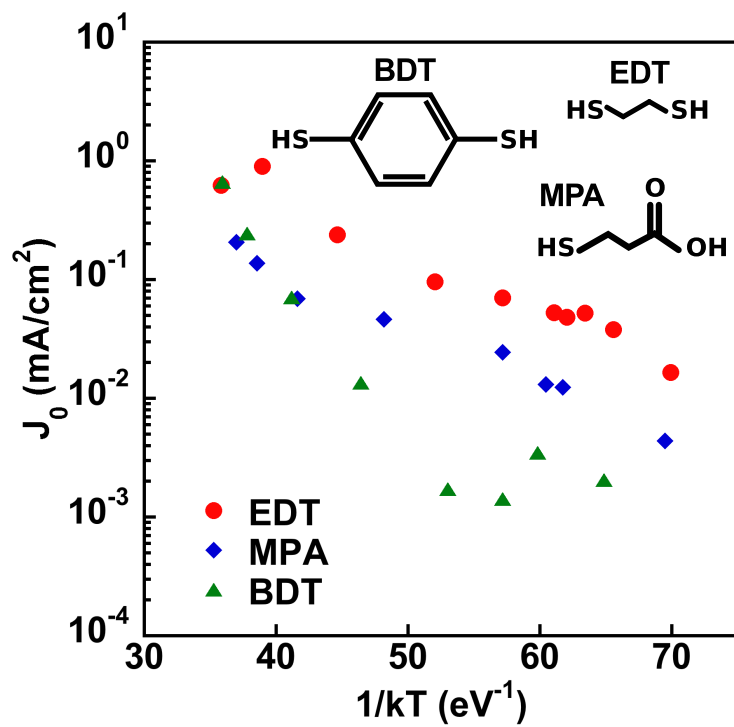
Figure 6.2: Arrhenius plot of the saturation current density for each ligand showing the negatively sloping linear behavior. Inset: The chemical structures of the three capping ligands studied herein.

6.3   Results

The transport mechanism of the devices was determined by fitting dark J-V data to the non-ideal diode equation

$$J(V) = J_0[\exp(A \times V) - 1] \tag{6.1}$$

where J_0 is the saturation current density and A is the exponential pre-factor. Both diode parameters in Equation 6.1, J_0 and A can be temperature dependent, with the transport mechanism being determined by the way in which they vary with temperature [18]. Figure 6.1 demonstrates the weak temperature dependence of A as plotted against $1/kT$. This, together with the negatively sloping linear behavior of J_0 in the Arrhenius plot of Figure 6.2, is characteristic evidence of tunneling transport [50].

Figure 6.3 shows dark and light current density versus voltage (J-V) data for an EDT device at a range of temperatures from 166 K to 324 K. The dark current density at a positive bias of 1 V shows two orders of magnitude increase from low to high temperatures, indicating that thermally excited charge carriers play an important role in conduction as T increases [60]. There is no appreciable distinction between dark J-V data from devices fabricated with the different ligands studied herein.

Under illumination, the ligand dependence of the devices is apparent in the PV parameters' temperature variations. Figure 6.4 shows the open-circuit voltage (V_{oc}) at a range of temperatures for devices using the three ligands. V_{oc} is expected to vary linearly with temperature [24]. However, a clear change in slope occurs when passing
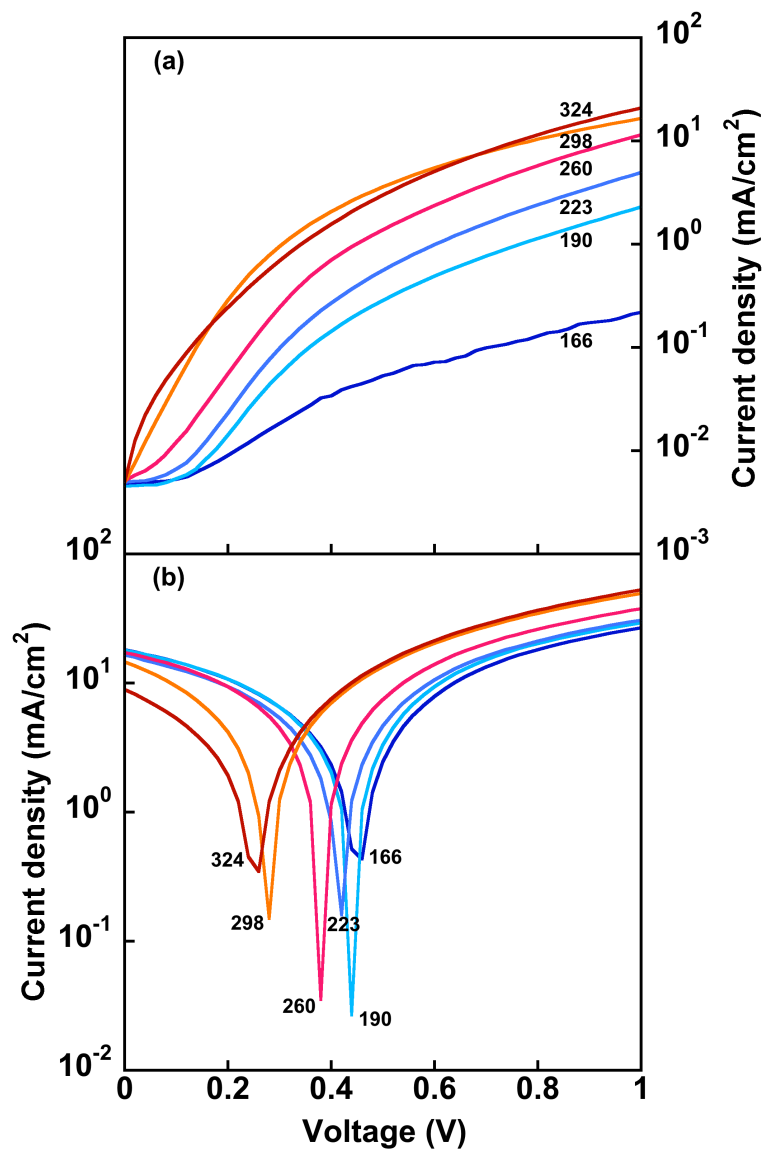
97

Figure 6.3: Current density-voltage data of an EDT device taken at 166, 190, 223, 260, 298 and 324 K. (a) Dark *J-V* measurements. (b) J-V measurements under illumination. (Absolute temperatures are indicated on each *J-V* curve.)
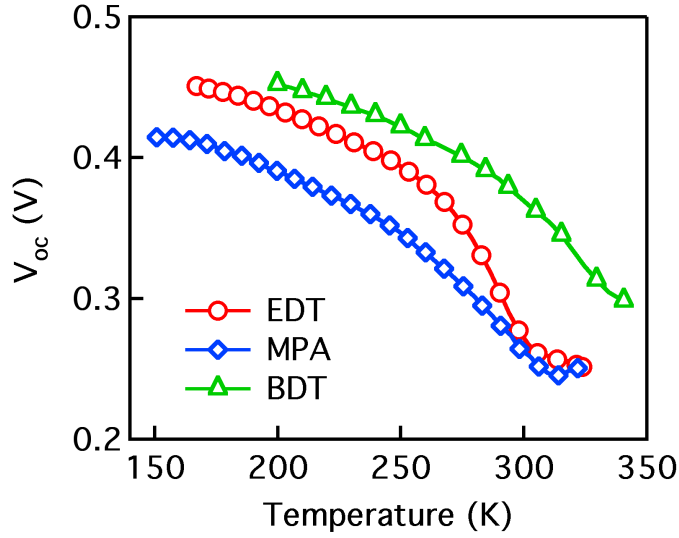
Figure 6.4: Open-circuit voltage dependence on temperature for three ligand devices. Extrapolating the flatter, low-temperature region yields built-in potential values for EDT, MPA and BDT devices (see text).

through room temperature for the EDT and MPA devices. BDT devices show the most linear V_{oc}-temperature dependence. The small change that does occur is seen at higher temperatures than in the EDT and MPA devices.

Extrapolation of V_{oc}-T data to 0 K provides the built-in potential (V_{bi}) of the devices [24], which indicates the difference in quasi-Fermi voltages between the $TiO_2$and PbS layers. The V_{bi} for EDT, MPA and BDT devices are 0.59±0.02 V, 0.56±0.03 V and 0.57±0.02 V respectively, indicating no significant ligand dependence of V_{bi}.

The shortcircuit current (J_{sc}) plotted as a function of temperature is shown in Figure 6.5. As with V_{oc}, both EDT and MPA exhibit a sharper change in J_{sc} than BDT. Both parameters' weaker dependence on temperature for BDT devices may be explained by BDT's more rigid structure. Comparing high-temperature to low-temperature J_{sc} val-
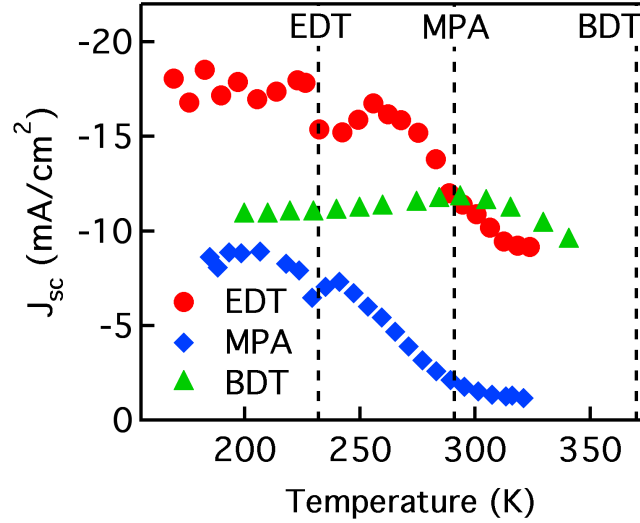
Figure 6.5: The variation of short-circuit current density with temperature for the three ligand devices. Vertical dashed lines show the melting point of each ligand.

ues, the absolute change is similar for both EDT and MPA, however MPA shows an approximately eight-fold increase while EDT is closer to two-fold. BDT is relatively flat through the temperature range, though the shallow increase upon warming from below room temperature is consistent with previous results [61].

In FF-temperature data for the three ligand devices, both EDT and BDT are relatively temperature-independent (around 25%), while MPA sharply rises above room temperature from less than 20% to more than 35%. This is markedly different than the ligand-dependence shown in both J_{sc}-and V_{oc}-temperature data. The steep increase in FF occurs with a simultaneous rise in shunt resistance for MPA devices, as seen in Figure 6.6. Both of these together, however, do not lead to better device performance at high temperatures, mainly due to the low J_{sc} and V_{oc} values. This is demonstrated
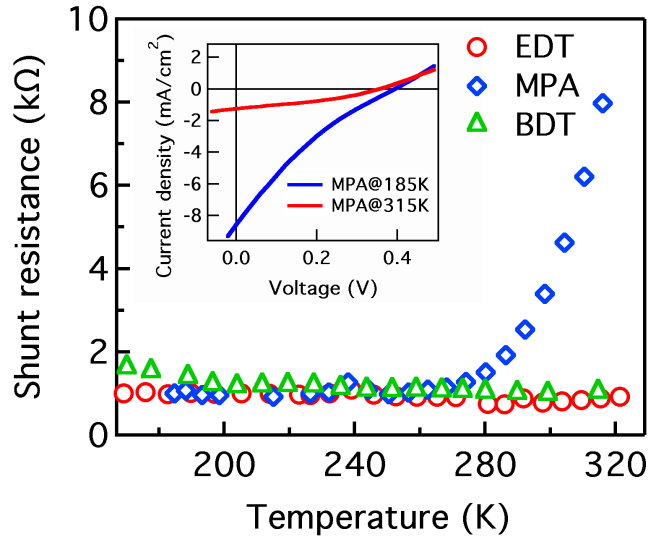
Figure 6.6: The shunt resistance dependence on temperature, showing MPA devices'large increase above room temperature.

in Figure 6.7, showing J-V data for all three ligands at both 185 K and 315 K. The large R_{sh} for the MPA device at a high temperature is clearly the poorest performing J-V curve. It is also seen in Figure 6.7 that the device made with EDT demonstrates the best EQE at low temperatures as well as a significant thermal shift compared to MPA and, especially, BDT.

6.4 Discussion

The discrepancy between dark and light current densities' response to cooling, as seen in the decrease in positive-bias current density in Figure 6.3 and the increase in J_{sc} in Figure 6.5, can be reconciled by considering the weaker role of deep trap states under illumination. This can be verified by measuring an ideality factor of unity, indi-

Figure 6.7: *J-V* characteristics for the photovoltaic devices fabricated with each of the three different ligands measured in the cryostat under illumination at both low temperature (185 K) and high temperature (315 K).

cating a direct, band-to-band recombination mechanism dominating transport, rather than recombination with charges in deep trap states. Attempting to obtain ideality factor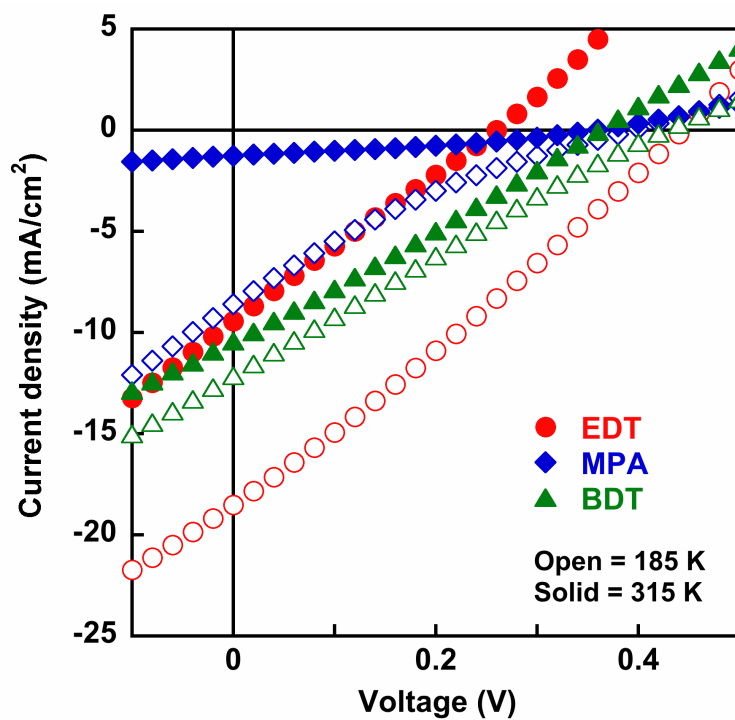s for the devices using the dark current density from Equation 6.1 yields nonunity values across the temperature range, leading us to believe that deep trap states play an important role in dark charge transport, which was previously seen to inhibit charge transport in PbS devices [62]. However, when examining devices under illumination, one may look at V_{oc} variations with light intensity, which should follow a linear trend on a semi-logarithmic plot, with the slope being the ideality factor in units of thermal voltage [52]. We obtain a near unity ideality factor of 1.01 when using this technique, indicating that deep traps no longer play a significant role under illumination, which can be explained by the increased number of charge carriers filling the traps leaving mainly direct recombination processes when illuminated [52].

J_{sc} dependence on temperature can partly be explained by the ligands freezing upon cooling. Previous studies have shown that ligand contraction in CdSe NP films lead to an order of magnitude decrease in transient times [63]. By varying the device ligand, we are able to verify that the freezing of the ligand does play a role in the PV properties of devices; however, not as clearly as this effect would suggest. With MPA's melting point being near room temperature (291 K), much higher than EDT at 232 K and BDT's being significantly higher than that at 370 K, we should observe J_{sc} peaks at different temperatures based on which ligand is being used. This was not the case, as seen in Figure 6.5, although BDT does display significantly different behavior. This difference may be attributed to the presence of a stiff benzene ring rather than the loose

103

carbon chains found in EDT and MPA (cf. Figure 6.2 inset). The stability of the ring translates to much smaller changes in device performance upon cooling since the ligand is less susceptible to temperature variations.

6.5   Conclusion

In summary, we have measured the effect of capping ligands in PbS NP ultra-thin film photovoltaic devices at varying temperatures through current-voltage measurements. Short-circuit current density and open- circuit voltage show similar variations with temperature for EDT and MPA devices, both exhibiting an increase upon cooling below room temperature. J_{sc} and V_{oc} for BDT devices are relatively temperature independent, which we attribute to the stiffness of the benzene ring compared to linear carbon chains. MPA devices demonstrate a sharp increase in fill factor and shunt resistance upon warming through room temperature, however device performance is not improved due to the poor fill factor of MPA devices at warmer temperatures. The increase in dark current density upon warming is attributed to the significant role played by trap states, while light current density decreasing with higher temperatures is caused by the ligand contraction and saturation of trap states by the increased density of charge carriers when illuminated. These results indicate that even higher performance should be achievable through the careful selection of the coupling ligands.

Chapter 7

Ge Quantum Dot Photovoltaic Devices

7.1   Introduction

We present our studies of germanium nanoparticle photovoltaic devices fabricated in a layered structure via spin-coating of the colloidal Ge solution. These devices provide potentially low-cost alternatives to conventional PV devices while requiring a less energy-intensive fabrication process and lower toxicity materials. We previously observed large forward-bias currents in Ge quantum dot solar cells. Here we demonstrate the performance of recent devices which exhibit a non-zero photocurrent in conjunction with a significant open-circuit voltage. Through temperature-dependent current-voltage measurements we extract the built-in potential and evidence for the dominant electron conduction mechanism. These preliminary results provide insight into the device band structure, allowing for future exploration of device manufacturing parameter space whereby modifications can further increase performance.

7.2 Device Structure

The unoptimized device structure is based on that which provides our highest quality PbS solar cells [53]. The layers are identical, switching PbS quantum dots for Ge, with a different capping ligand.

Light enters the device through a glass slide, which is pre-patterned with a transparent conducting oxide (TCO). Two TCOs are compared herein: fluorinated tin oxide (FTO) and indium-doped tin oxide (ITO). A sol-gel layer of TiO_2 acts as a buffer between the pre-patterned TCO and the mesoporous nanoparticle layer of TiO_2. This is to prevent shorting caused by the sharp surface of the TCO layer, which is potentially able to shunt through to the back contact. Both TiO_2 layers are spun on from solution and sintered in air at 450°C. TiO_2 is a large band gap semiconductor, transparent to the optical spectrum, and therefore acts as the window layer in QD devices. It is well understood to be a strong electrical conductor and is therefore acting as the n-type layer of the p-n heterojunction.

Light is absorbed in the germanium quantum dot layer. The colloidal solution of Germanium NPs capped with oleylamine is spun on or dip-coated in a nitrogen environment, followed by a ligand exchange with hydrazine replacing the longer oleylamine chains. This ligand exchange is necessary to allow shorter QD separation on the films, enhancing electrical conduction.

Silver is thermally evaporated as the back contact. This metal is chosen for its near matching with the HOMO level of Ge QDs, leading to a good Ohmic contact as
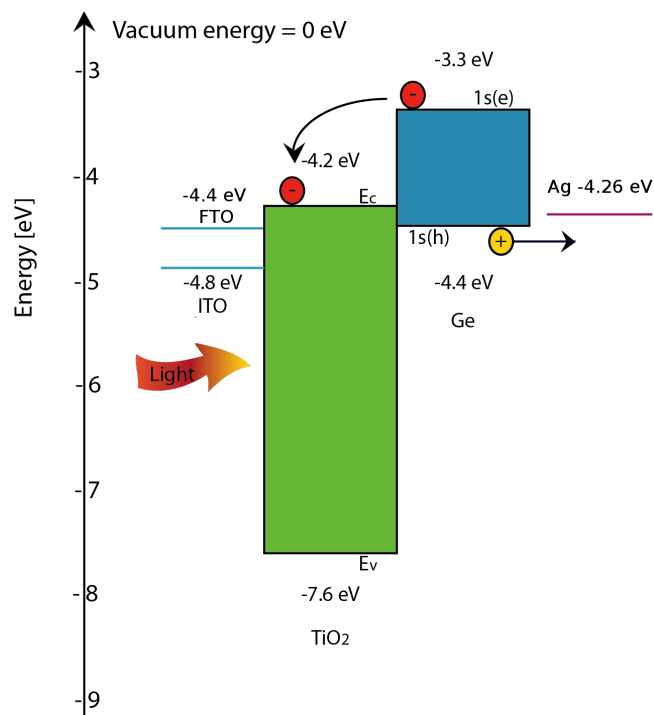
Vacuum energy = 0 eV

Energy [eV]

-3.3 eV
1s(e)

-4.2 eV

-4.4 eV
FTO

E_c

Ag -4.26 eV

1s(h)

-4.8 eV
ITO

-4.4 eV

Ge

Light

E_v

-7.6 eV

TiO$_2$

Figure 7.1: The flat-band energy diagram of the Ge/TiO$_2$ QD heterojunction photovoltaic device. Both transparent conducting oxides' workfunctions are shown for comparison.

an efficient hole collector. The flat band diagram for the complete Ge device is shown in Figure 7.1 with a schematic view of the device presented in Figure 7.2.

Devices remain in an inert atmosphere until transfer into the cryostat, at which point they are exposed to air for ~5 minutes while in transit. The effects of this air exposure are explored below.

7.3 Quantum Dot Synthesis

Germanium nanoparticles were synthesized via microwave heating of GeI$_2$/GeI$_4$ solutions, the ratio of which controlling nanoparticle size and thereby the peak absorp-
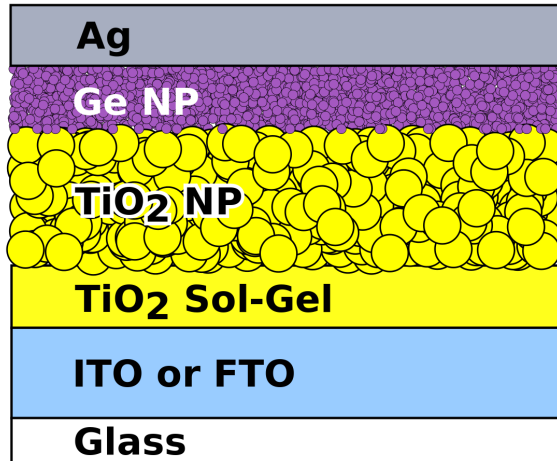
Figure 7.2: A schematic view of the layered structure. Light enters from below, through the glass, TCO, and window layers before reaching the active NP layer.

tion wavelength [45]. The quantum dots utilized herein are ~4 nm in diameter corresponding to an exciton peak of 1.1 eV photons [46]. This is near the Shockley-Queisser peak photo-absorption band gap from an AM1.5 spectrum [21].

7.4 Transparent Conducting Oxide

Working devices were fabricated using two types of transparent conducting oxides: indium tin oxide (ITO) and fluorine-doped tin oxide (FTO). A comparison of both front-contact materials exhibit small differences on device parameters—FTO yielding a slightly better J_{sc} while ITO provides slightly higher V_{oc} values. Devices fabricated with FTO offer a bit higher current densities in conjunction with an order of magnitude improvement in rectification. The two TCOs effect on J-V data under illumination are shown in Figure 7.3. Dark and light data is presented in the log plot of Figure 7.4. Temperature-dependent current-voltage measurements herein utilize devices
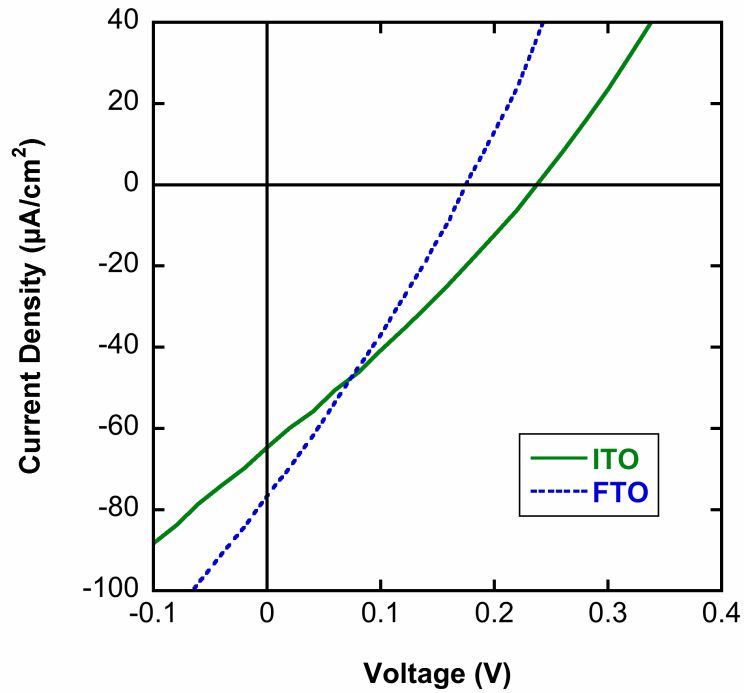
Figure 7.3: Current density-voltage curves for Ge devices under AM1.5G illumination with two different transparent conducting oxides.

made with FTO as the front contact.

7.5   Temperature-Dependent Current-Voltage

As stated above, devices are exposed to air for ~5 minutes between being removed from the nitrogen environment of the glove box and being placed in the cryostat. The cryostat uses an overpressure of nitrogen gas which flows across the device, preventing ambient air from entering the central column and reaching the device.

Cryostat cooling is performed by liquid N_2 and warmed by a resistive heater. Temperature is monitored through a calibrated RTD sensor. Devices are illuminated

Figure 7.4: Semilog plot of *J-V* data comparing the two TCOs in both dark and illuminated conditions.
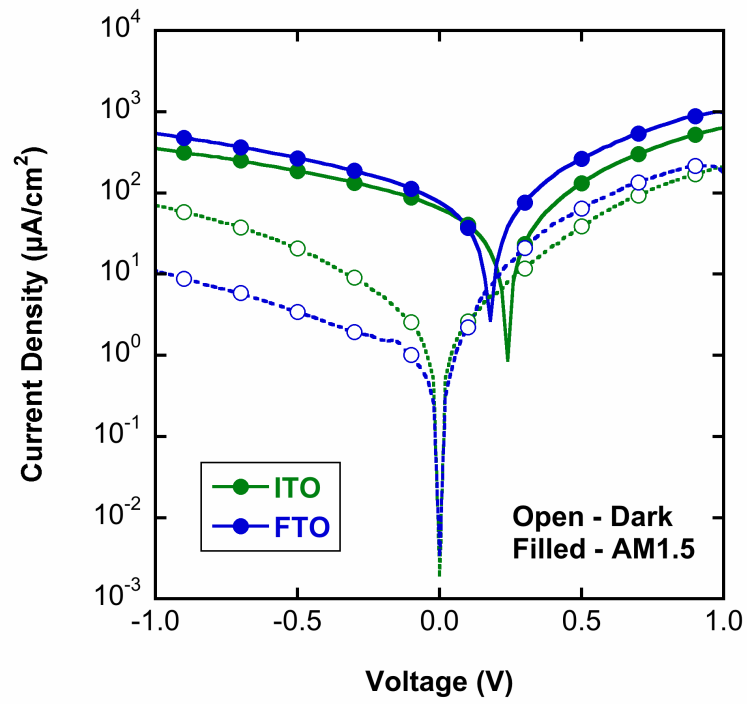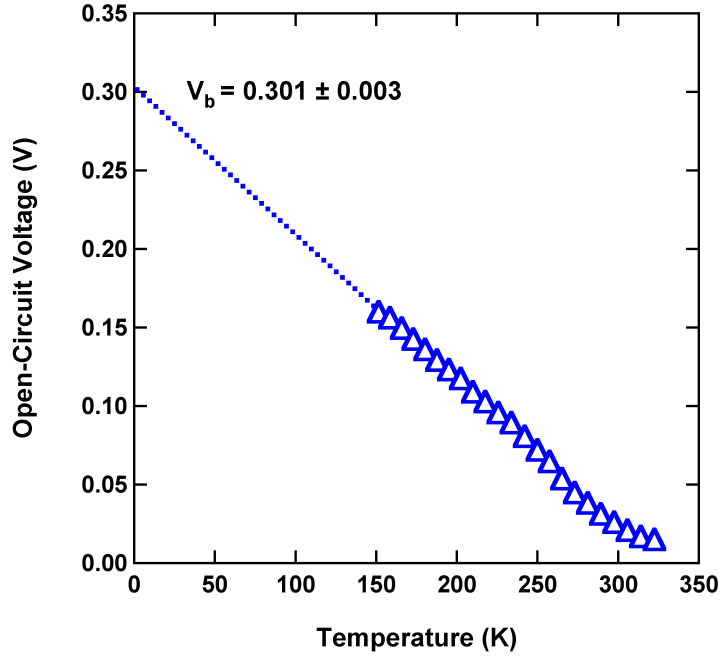
Figure 7.5: The open-circuit voltage at a range of temperatures for a Ge device. The extrapolated linear trend intercepts $T=0$ at the barrier height as shown.

by a xenon bulb, which sits adjacent to the device while in the cryostat. The bulb loses calibration below 150 K thereby limiting the lower temperature range.

While at a range of temperatures, full J-V curves are taken from -1 to +1 V. This provides useful solar cell device figures of merit. Extrapolation of V_{oc} to $T=0$ K provides the barrier height which is 0.301±0.003 V for these devices. The V_{oc}-T and J_{sc}-T data are shown in Figures 7.5 and 7.6, respectively.

From the slope of J-V data at J_{sc} and V_{oc}, the shunt and series resistances, respectively, can be extracted, which are presented in Figure 7.7. The bifurcation of series and shunt resistances corresponds to an increase in fill factor at lower temperatures to >30%.

111
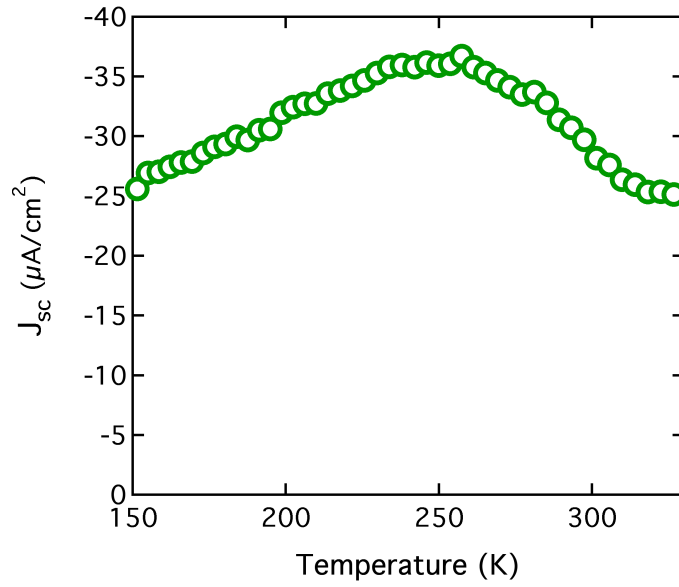
Figure 7.6: The short-circuit current density for a Ge device as a function of temperature.
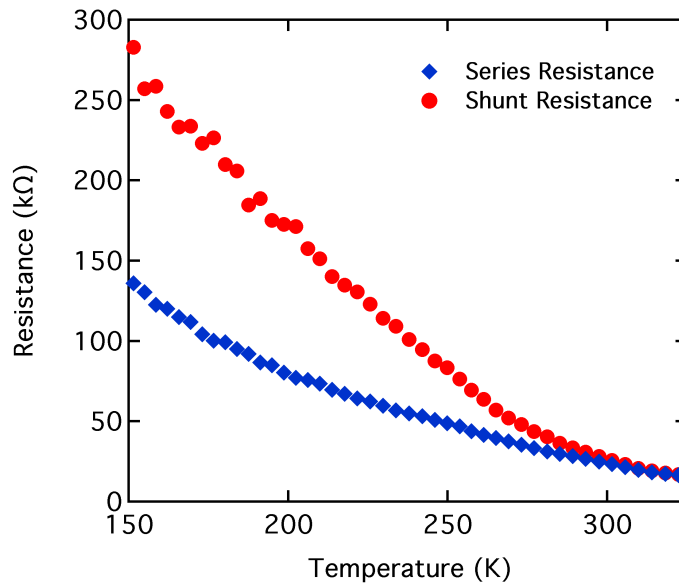
Figure 7.7: The bifurcation of the series and shunt resistances in Ge devices, corresponding to an increased fill factor at lower temperatures.
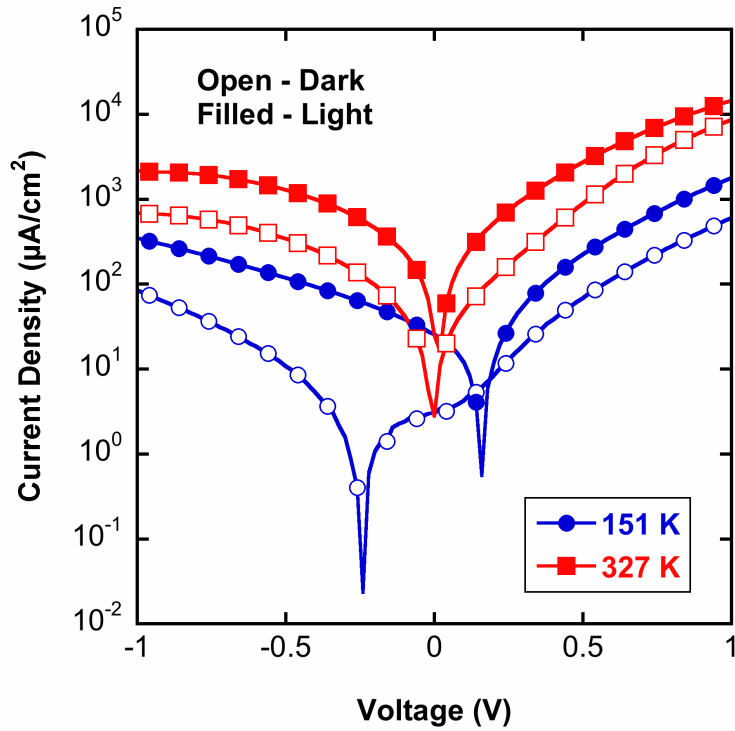
Figure 7.8: Current-voltage data from a Ge device at the temperature extremes studied herein. Both illuminated and dark dark data are shown for comparison.

Comparing the dark and light data at the high and low extremes of temperatures reached in the cryostat, clearly at the high T of 327 K the current density is an order of magnitude stronger than at 151 K. This indicates that thermally activated charge carriers are playing an important role. However, the lower dark current at low temperatures leads to a high V_{oc}. Both high and low, dark and light J-V data are presented in the log plot of Figure 7.8.

113

7.6 Air Exposure Analysis

Previous results with PbS QD devices indicated an improvement after brief air exposure. In the present study, Ge devices are exposed to air while in transit from the glovebox to the cryostat. In trying to separate performance degradation due to temperature variations from those due to air exposure, a systematic study is presented.

Air exposure was performed under laboratory fluorescent lighting for the indicated times. After each period, the device was placed back in the nitrogen glovebox where it was measured using the solar simulator. In removing and replacing the device in the glovebox, there is a brief exposure to vacuum while in the antechamber. This was shown to not have an effect on performance.

The results of air exposure are shown in Figure 7.9. Devices exhibit a steep initial decrease in performance after brief removal from inert glovebox environment. V_{oc} regains much of its original value over 24 hours of air exposure, however J_{sc} drops dramatically over the same period.

Our previous PbS QD PV results indicate regenerative effect of soaking in capping ligand solution. This was attributed to the dissociation of the ligand from oxygen's bond replacing that of the thiol ligand. However, the Ge device performance degrades after a similar procedure, resoaking devices in hydrazine for 5 minutes. A longer hydrazine soak provides no added benefit.
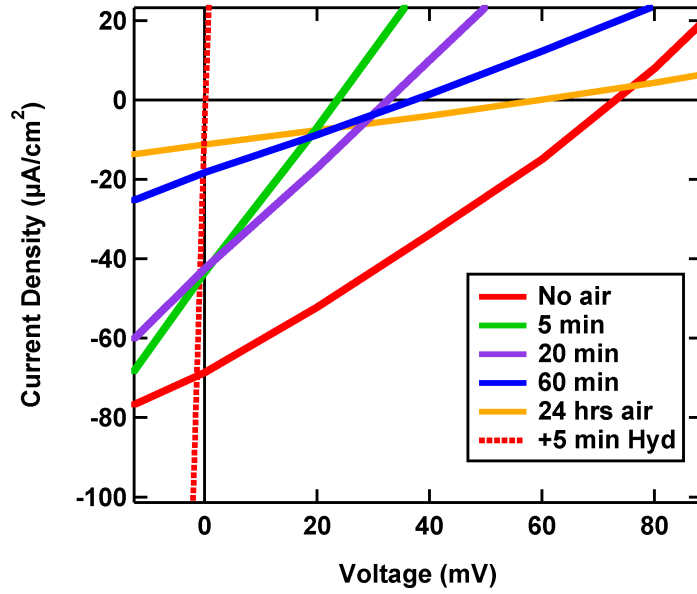
Figure 7.9: Prolonged air exposure for Ge devices degrades device performance. After an initial sharp V_{oc} decline, much is recovered after a day's exposure to air. A ligand soak has a detrimental effect on device performance.

7.7   Electron Transport

In measuring J-V data at varying temperatures dark curves are fit to an non-ideal diode equation given by

$$J(V) = J_0[\exp(A \times V) - 1], \tag{7.1}$$

where $J_0(T)$ is the reverse saturation current density and $A(T)$ is an exponential pre-factor, which is similar to the ideality factor n. Both fitting parameters J_0 and A can be dependent upon temperature, the way in which suggesting the dominant transport mechanism. Fitting is performed by least squares method. The results of the fitting are

115
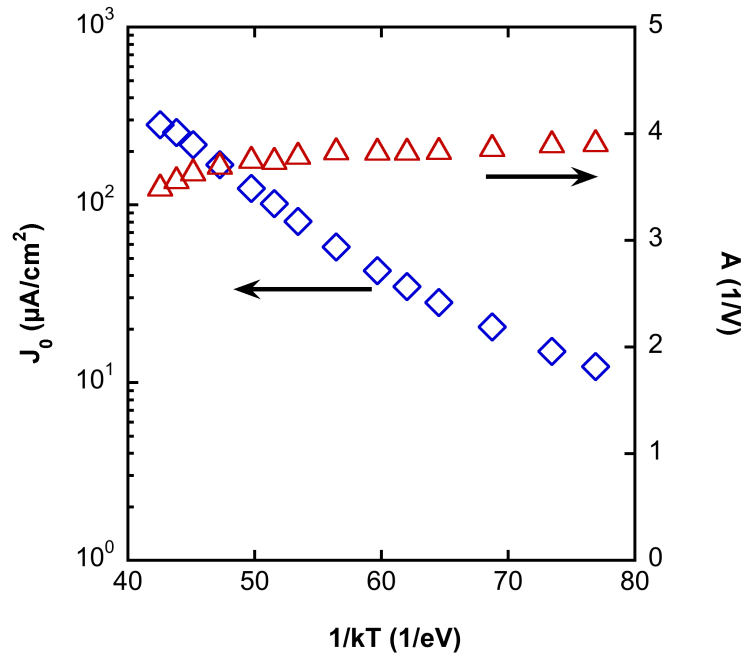
Figure 7.10: Diode fit parameters from Equation 7.1. The parameters' temperature dependence together indicate tunneling transport dominating electron conduction.

shown in Figure 7.10. The linear J_0 behavior in an Arrhenius plot along with constant A indicates tunneling transport through the device interface.

7.8 Conclusion

We have fabricated working germanium nanoparticle photovoltaic devices with open-circuit voltages around 200 mV. Both ITO and FTO provide working contacts, with benefits and drawbacks to both choices. Damage caused by air exposure is unable to be recovered through ligand-solution soaking. Electron transport is dominated by tunneling transport. Despite low short-circuit current densities, these preliminary results offer insight into band alignment factors—namely the TiO_2/Ge barrier potential—that,

once tuned, could provide higher photoconversion efficiencies.

Chapter 8

Conclusion

As we reach the point where choices decide the quality of the next generation's environmental health, a new approach is needed to bring down the cost of photovoltaics if it is to ever have a chance of significantly displacing carbon-burning alternatives. Even with the recent drop in silicon solar module costs, more work is needed, especially with an at least equally dramatic shift in natural gas prices. Quantum dot photovoltaics could potentially provide a solutions. With much less material required, and lower temperatures of device manufacturing, the front end costs are potentially much lower than other technologies. In addition, multiple exciton generation and the simplicity of graded band gaps fabrication could drive the efficiencies beyond the Shockley-Queisser limit.

This dissertation attempted to answer fundamental questions of the electron transport mechanisms within these QD PV devices. By understanding how the diode behaves in the dark, PV parameters which are a result of basic diode performance

could be further optimized. Furthermore, the way in which these parameters vary with temperature allows a better understanding of device operation.

Temperature dependent electron transport is a valuable way to see through the murky waters of disordered systems of these QD thin-film devices. Through further studies that explore the vast parameter space of transport and optical properties, eventually QD PV could find its place on future rooftops.

Bibliography

[1] Richard P Feynman. There's plenty of room at the bottom. *Engineering and Science*, 23(5):22–36, 1960.

[2] I Carbone, Q Zhou, B Vollbrecht, L Yang, S Medling, A Bezryadina, F Bridges, GB Alers, JT Norman, and T Kinmen. Pulsed chemical vapor deposition of cu_2s into a porous tio_2 matrix. *Journal of Vacuum Science & Technology A: Vacuum, Surfaces, and Films*, 29(5):051505–051505, 2011.

[3] C Vieu, F Carcenac, A Pepin, Y Chen, M Mejias, A Lebib, L Manin-Ferlazzo, L Couraud, and H Launois. Electron beam lithography: resolution limits and applications. *Applied Surface Science*, 164(1):111–117, 2000.

[4] Gerd Binnig, Heinrich Rohrer, Ch Gerber, and E Weibel. Tunneling through a controllable vacuum gap. *Applied Physics Letters*, 40(2):178–180, 1982.

[5] Donald M Eigler and Erhard K Schweizer. Positioning single atoms with a scanning tunnelling microscope. *Nature*, 344(6266):524–526, 1990.

[6] R de L Kronig and WG Penney. Quantum mechanics of electrons in crystal lattices. *Proceedings of the Royal Society of London. Series A*, 130(814):499–513, 1931.

[7] David Jeffery Griffiths. *Introduction To Quantum Mechanics, 2/E*. Pearson Education, 2005.

[8] A. Kitai. *Principles of Solar Cells, LEDs and Diodes*. John Wiley and Sons, Bellingham, Washington, USA, 2011.

[9] Debasis Bera, Lei Qian, Teng-Kuan Tseng, and Paul H Holloway. Quantum dots and their multimodal applications: a review. *Materials*, 3(4):2260–2345, 2010.

[10] CBea Murray, DJ Norris, and Moungi G Bawendi. Synthesis and characterization of nearly monodisperse cde (e= sulfur, selenium, tellurium) semiconductor nanocrystallites. *Journal of the American Chemical Society*, 115(19):8706–8715, 1993.

[11] Michael L Steigerwald and Louis E Brus. Semiconductor crystallites: a class of large molecules. *Accounts of Chemical Research*, 23(6):183–188, 1990.

[12] A Paul Alivisatos. Perspectives on the physical chemistry of semiconductor nanocrystals. *The Journal of Physical Chemistry*, 100(31):13226–13239, 1996.

[13] DJ Norris and MG Bawendi. Measurement and assignment of the size-dependent optical spectrum in cdse quantum dots. *Physical Review B*, 53(24):16338, 1996.

[14] Ying Wang and N Herron. Nanometer-sized semiconductor clusters: materials syn-

thesis, quantum size effects, and photophysical properties. *The Journal of Physical Chemistry*, 95(2):525–532, 1991.

[15] Jungsik Bang, Heesun Yang, and Paul H Holloway. Enhanced and stable green emission of zno nanoparticles by surface segregation of mg. *Nanotechnology*, 17(4):973, 2006.

[16] Qiang Wang, Yuching Kuo, Yuwen Wang, Gyehwa Shin, Chada Ruengruglikit, and Qingrong Huang. Luminescent properties of water-soluble denatured bovine serum albumin-coated cdte quantum dots. *The Journal of Physical Chemistry B*, 110(34):16860–16866, 2006.

[17] G Horowitz, R Hajlaoui, R Bourguiga, and M Hajlaoui. Theory of the organic field-effect transistor. *Synthetic metals*, 101(1):401–404, 1999.

[18] LF Marsal, J. Pallares, X. Correig, A. Orpella, D. Bardés, and R. Alcubilla. Analysis of conduction mechanisms in annealed n-si1- xcx: H/p-crystalline si heterojunction diodes for different doping concentrations. *Journal of applied physics*, 85(2):1216–1221, 1999.

[19] LF Marsal, I Martin, J Pallares, A Orpella, and R Alcubilla. Annealing effects on the conduction mechanisms of p-amorphous-sic: H/n-crystalline-si diodes. *Journal of applied physics*, 94:2622, 2003.

[20] William Shockley and Hans J Queisser. Detailed balance limit of efficiency of p-n junction solar cells. *Journal of Applied Physics*, 32(3):510–519, 1961.

[21] Thomas Kirchartz, K Ding, and U Rau. *Advanced Characterization Techniques for Thin Film Solar Cells.* Wiley-VCH Verlag GmbH & Co. KGaA New York, 2011.

[22] P Wurfel. The chemical potential of radiation. *Journal of Physics C: Solid State Physics*, 15(18):3967, 1982.

[23] Charles H Henry. Limiting efficiencies of ideal single and multiple energy gap terrestrial solar cells. *Journal of applied physics*, 51(8):4494–4500, 1980.

[24] Steven S Hegedus and William N Shafarman. Thin-film solar cells: device measurements and analysis. *Progress in Photovoltaics: Research and Applications*, 12(2-3):155–176, 2004.

[25] Richard Williams. Becquerel photovoltaic effect in binary compounds. *The Journal of Chemical Physics*, 32:1505, 1960.

[26] Martin A Green. Photovoltaics: Coming of age. In *Photovoltaic Specialists Conference, 1990., Conference Record of the Twenty First IEEE*, pages 1–8. IEEE, 1990.

[27] DM Chapin, CS Fuller, and GL Pearson. A new silicon p-n junction photocell for converting solar radiation into electrical power. *Journal of Applied Physics*, 25(5):676–677, 1954.

[28] MA Green, J Zhao, A Wang, and SR Wenham. Progress and outlook for high-efficiency crystalline silicon solar cells. *Solar Energy Materials and Solar Cells*, 65(1):9–16, 2001.

[29] RB Bergmann. Crystalline si thin-film solar cells: a review. *Applied physics A*, 69(2):187–194, 1999.

[30] S Guha, J Yang, A Banerjee, T Glatfelter, K Hoffman, SR Ovshinsky, M Izu, HC Ovshinsky, and X Deng. Amorphous silicon alloy photovoltaic technology-from r&d to production. In *MRS Proceedings*, volume 345. Cambridge Univ Press, 1994.

[31] Chetan Singh Solanki. *Solar Photovaltaics*. PHI Learning Pvt. Ltd., 2011.

[32] Narayanan Komerath, Vigneshwar Venkat, and Abhizna Butchibabu. Parameter selection for a space power grid. *AIAA*, 7711:2008, 2008.

[33] Iwan Moreels, Karel Lambert, Dries Smeets, David De Muynck, Tom Nollet, José C Martins, Frank Vanhaecke, Andre Vantomme, Christophe Delerue, Guy Allan, et al. Size-dependent optical properties of colloidal pbs quantum dots. *Acs Nano*, 3(10):3023–3030, 2009.

[34] Steven A Mcdonald, Gerasimos Konstantatos, Shiguo Zhang, Paul W Cyr, Ethan JD Klem, Larissa Levina, and Edward H Sargent. Solution-processed pbs quantum dot infrared photodetectors and photovoltaics. *Nature materials*, 4(2):138–142, 2005.

[35] Alexander H Ip, Susanna M Thon, Sjoerd Hoogland, Oleksandr Voznyy, David Zhitomirsky, Ratan Debnath, Larissa Levina, Lisa R Rollny, Graham H Carey,

Armin Fischer, et al. Hybrid passivated colloidal quantum dot solids. *Nature nanotechnology*, 2012.

[36] Ethan JD Klem, Dean D MacNeil, Paul W Cyr, Larissa Levina, and Edward H Sargent. Efficient solution-processed infrared photovoltaic cells: Planarized all-inorganic bulk heterojunction devices via inter-quantum-dot bridging during growth from solution. *Applied physics letters*, 90(18):183113–183113, 2007.

[37] Jason P Clifford, Keith W Johnston, Larissa Levina, and Edward H Sargent. Schottky barriers to colloidal quantum dot films. *Applied Physics Letters*, 91(25):253117–253117, 2007.

[38] Keith W Johnston, Andras G Pattantyus-Abraham, Jason P Clifford, Stefan H Myrskog, Dean D MacNeil, Larissa Levina, and Edward H Sargent. Schottky-quantum dot photovoltaics for efficient infrared power conversion. *Applied Physics Letters*, 92(15):151115–151115, 2008.

[39] Wanli Ma, Sarah L Swisher, Trevor Ewers, Jesse Engel, Vivian E Ferry, Harry A Atwater, and A Paul Alivisatos. Photovoltaic performance of ultrasmall pbse quantum dots. *ACS nano*, 5(10):8140–8147, 2011.

[40] Andras G Pattantyus-Abraham, Illan J Kramer, Aaron R Barkhouse, Xihua Wang, Gerasimos Konstantatos, Ratan Debnath, Larissa Levina, Ines Raabe, Mohammad K Nazeeruddin, Michael Gratzel, et al. Depleted-heterojunction colloidal quantum dot solar cells. *ACS nano*, 4(6):3374–3380, 2010.

[41] Xihua Wang, Ghada I Koleilat, Jiang Tang, Huan Liu, Illan J Kramer, Ratan Debnath, Lukasz Brzozowski, D Aaron R Barkhouse, Larissa Levina, Sjoerd Hoogland, et al. Tandem colloidal quantum dot solar cells employing a graded recombination layer. *Nature Photonics*, 5(8):480–484, 2011.

[42] Edward H Sargent. Colloidal quantum dot solar cells. *Nature Photonics*, 6(3):133–135, 2012.

[43] I.J. Kramer, A.G. Pattantyus-Abraham, A.R. Barkhouse, X. Wang, G. Konstantatos, R. Debnath, L. Levina, I. Raabe, M.K. Nazeeruddin, M. Grätzel, et al. Advances in colloidal quantum dot solar cells: The depleted-heterojunction device. *Thin Solid Films*, 519(21):7351–7355, 2011.

[44] JamesáR Heath. Covalency in semiconductor quantum dots. *Chemical Society Reviews*, 27(1):65–71, 1998.

[45] Elayaraja Muthuswamy, Andrew S Iskandar, Marlene M Amador, and Susan M Kauzlarich. Facile synthesis of germanium nanoparticles with size control: Microwave versus conventional heating. *Chemistry of Materials*, 2012.

[46] C Bostedt, T Van Buuren, TM Willey, N Franco, LJ Terminello, C Heske, and T Moller. Strong quantum-confinement effects in the conduction band of germanium nanocrystals. *Applied physics letters*, 84(20):4056–4058, 2004.

[47] G. Zhai, A. Bezryadina, A.J. Breeze, D. Zhang, G.B. Alers, and S.A. Carter. Air

stability of tio2/pbs colloidal nanoparticle solar cells and its impact on power efficiency. *Applied Physics Letters*, 99:063512, 2011.

[48] Dieter K Schroder. *Semiconductor material and device characterization.* Wiley-interscience, 2006.

[49] Hideharu Matsuura. Hydrogenated amorphous-silicon/crystalline-silicon hetero-junctions: properties and applications. *Electron Devices, IEEE Transactions on*, 36(12):2908–2914, 1989.

[50] Sangwook Park, Eunchel Cho, Dengyuan Song, Gavin Conibeer, and Martin A Green. n-type silicon quantum dots and p-type crystalline silicon heteroface solar cells. *Solar Energy Materials and Solar Cells*, 93(6):684–690, 2009.

[51] EH Rhoderick and RH Williams. Metal–semiconductor contacts, 2nd edn. clarendon, 1988.

[52] Martijn Kuik, Herman T Nicolai, Martijn Lenes, Gert-Jan AH Wetzelaer, Mingtao Lu, and Paul WM Blom. Determination of the trap-assisted recombination strength in polymer light emitting diodes. *Applied Physics Letters*, 98(9):093301–093301, 2011.

[53] T. Ju, R.L. Graham, G. Zhai, Y.W. Rodriguez, A.J. Breeze, L. Yang, G.B. Alers, and S.A. Carter. High efficiency mesoporous titanium oxide pbs quantum dot solar cells at low temperature. *Applied Physics Letters*, 97(4):043106–043106, 2010.

[54] Randy J Ellingson, Matthew C Beard, Justin C Johnson, Pingrong Yu, Olga I

Micic, Arthur J Nozik, Andrew Shabaev, and Alexander L Efros. Highly efficient multiple exciton generation in colloidal pbse and pbs quantum dots. *Nano Letters*, 5(5):865–871, 2005.

[55] L Bakueva, S Musikhin, MA Hines, T-WF Chang, M Tzolov, GD Scholes, and EH Sargent. Size-tunable infrared (1000–1600 nm) electroluminescence from pbs quantum-dot nanocrystals in a semiconducting polymer. *Applied Physics Letters*, 82(17):2895–2897, 2003.

[56] Kwang S Jeong, Jiang Tang, Huan Liu, Jihye Kim, Andrew W Schaefer, Kyle Kemp, Larissa Levina, Xihua Wang, Sjoerd Hoogland, Ratan Debnath, et al. Enhanced mobility-lifetime products in pbs colloidal quantum dot photovoltaics. *ACS nano*, 6(1):89–99, 2011.

[57] Ghada I Koleilat, Larissa Levina, Harnik Shukla, Stefan H Myrskog, Sean Hinds, Andras G Pattantyus-Abraham, and Edward H Sargent. Efficient, stable infrared photovoltaics based on solution-cast colloidal quantum dots. *ACS nano*, 2(5):833–840, 2008.

[58] Joseph M Luther, Jianbo Gao, Matthew T Lloyd, Octavi E Semonin, Matthew C Beard, and Arthur J Nozik. Stability assessment on a 3% bilayer pbs/zno quantum dot heterojunction solar cell. *Advanced Materials*, 22(33):3704–3707, 2010.

[59] Nathan L Hammer, Todd S Emrick, and Michael D Barnes. Quantum dots coordi-

nated with conjugated organic ligands: new nanomaterials with novel photophysics. *Nanoscale Research Letters*, 2:282–290, 2007.

[60] Souvik Kundu, Sandip Kumar Roy, and P Banerji. Gaas metal–oxide–semiconductor device with titanium dioxide as dielectric layer: effect of oxide thickness on the device performance. *Journal of Physics D: Applied Physics*, 44(15):155104, 2011.

[61] Krisztina Szendrei, Mark Speirs, Widianta Gomulya, Dorota Jarzab, Marianna Manca, Oleksandr V Mikhnenko, Maksym Yarema, Bart J Kooi, Wolfgang Heiss, and Maria A Loi. Exploring the origin of the temperature-dependent behavior of pbs nanocrystal thin films and solar cells. *Advanced Functional Materials*, 22(8):1598–1605, 2012.

[62] D Aaron R Barkhouse, Andras G Pattantyus-Abraham, Larissa Levina, and Edward H Sargent. Thiols passivate recombination centers in colloidal quantum dots leading to enhanced photovoltaic device efficiency. *ACS nano*, 2(11):2356–2362, 2008.

[63] R. Loef, A.J. Houtepen, E. Talgorn, J. Schoonman, and A. Goossens. Temperature dependence of electron transport in cdse quantum dot films. *The Journal of Physical Chemistry C*, 113(36):15992–15996, 2009.